To the Graduate Council:

I am submitting herewith a thesis written by Cary Rock entitled "Search for Hidden Sectors With Neutrons." I have examined the final paper copy of this thesis for form and content and recommend that it be accepted in partial fulfillment of the requirements for the degree of Doctor of Philosophy, with a major in Physics.

Yuri Kamyshkov, Major Professor

We have read this thesis
and recommend its acceptance:

Lawrence Heilbronn

Yuri Efremenko

Christian Batista

Accepted for the Council:

Dixie L. Thompson

Vice Provost and Dean of the Graduate School

To the Graduate Council:

I am submitting herewith a thesis written by Cary Rock entitled "Search for Hidden Sectors With Neutrons." I have examined the final electronic copy of this thesis for form and content and recommend that it be accepted in partial fulfillment of the requirements for the degree of Doctor of Philosophy, with a major in Physics.

Yuri Kamyshkov, Major Professor

We have read this thesis
and recommend its acceptance:

Lawrence Heilbronn

Yuri Efremenko

Christian Batista

Accepted for the Council:

Dixie L. Thompson

Vice Provost and Dean of the Graduate School

(Original signatures are on file with official student records.)

Search for Hidden Sectors With Neutrons

A Dissertation Presented for the

Doctor of Philosophy

Degree

The University of Tennessee, Knoxville

Cary Rock

August 2025

To my parents, Alan and Suzanne, and my grandparents, Robert, Betty, Thurman, Patricia, and Sharon, but especially to Robert.

Acknowledgments

I would like to thank: my advisor, Yuri Kamyshkov, for being such a patient man; Adrian Del Maestro and Steve Johnston for pointing out where I was deficient; Alex Small for giving me a chance to see; and Kai Lam for showing me that there was so much more magic out there.

In addition, I would like to thank, in alphabetical order, the undergraduate students of the group for their work in calculating the HFIR 2024 experiment beam's initial intensity: Carolyn Haviland, James Rogers, and Nathan Whittington. I would also like to thank them for their work in identifying the dead time of the detector, the aggregated values for the runs, the various factors that feed into correcting the final counts of the experiment runs, and the preliminary calculations of the limit used for the numerical calculations. Further, I would like to thank former undergraduate Micheal Kline and ORNL staff scientists David Mathews and Frank Gonzalez for their work on the implementation of the simulation code used for the SNS 2020 and HFIR 2024 experiments.

I do not seek. I find.

- Pablo Picasso

This is a load of barnacles.

- Frank the Fish

Abstract

The fundamental nature of Dark Matter (DM) is heretofore entirely unknown. Interacting only gravitationally, to this form of matter is attributed many astronomical observations of behaviors astronomic. Explanations of DM abound, ranging from Weakly-Interacting Massive Particles (WIMPs) of a range of mass-energies from $\mathcal{O}$(100 GeV) [1] down to below $\mathcal{O}$(1e-20 eV) [17].

Mirror matter is a testable model for dark matter as well as a means of explaining the baryon asymmetry of the universe. Here I present my work on the analysis of two experiments performed at the Oak Ridge National Laboratory as well as a third-party analysis of an experiment performed at the Institut Laue-Langevin in Grenoble, France.

Table of Contents

Nomenclature

B	Baryon Number
L	Lepton Number
DM	Dark Matter
MM	Mirror Matter
OM	Ordinary Matter
SM	(Ordinary) Standard Model
SM’	Mirror-Symmetric Standard Model
SML	(Ordinary) Standard Model Lagrangian
VEV	Vacuum Expectation Value

Chapter 1

Introduction and Theory

The nature of Dark Matter (DM) is not at all understood. All that is truly known about it at this time is that it does not interact electromagnetically, does not emit light that our detectors have been able to record, and seems to only interact gravitationally. These being the case, it is not even known if it is a particle, let alone where it might fit into a model such as the Standard Model (SM - for a review from textbooks, see such as [25], [34], [10], or from lectures from such as by [29]). However, in order to consider an experiment or design a detector for DM, assumptions about its nature must be made. It is entirely reasonable to assume that ”Dark Matter” is ”matter”, but to do so and still make sensible predictions that fit with observations, it must be understood that it might not be a particle that fits into the SM as it is known today.

This introduction will begin by summarizing the motivating factors for Dark Matter, how DM might explain the Baryon asymmetry observed in the universe today, a model (”Mirror Matter”) that has explanatory power for some of the observations where DM is employed, an alternative foundation for the same model, followed by overviews of experiment types and results in order to detect or set limits on the Mirror Matter model's predicted particles. In **Chapter 3**, an analysis that was performed on data that was obtained from an experiment at the Spallation Neutron Source (SNS) at Oak Ridge National Lab (ORNL) in 2020 is detailed. **Chapter 4** contains a similar analysis for an experiment performed in 2024 at the High Flux Isotope Reactor (HFIR), also at ORNL. **Chapter 5** contains a third-party, very-rough analysis of the results of another group (the STEREO collaboration) from an experiment (the STEREO experiment proper) performed at the High Flux Reactor (RHF) at the Institut Laue-Langevin (ILL) in Grenoble, France as a consideration of the feasibility of the claims.

1.1 Motivating Factors

Cosmological and astronomical observations [18, 30, 36] have indicated interactions that are gravitational in nature with no electromagnetic signature associated. The assumed cause of these interactions is a hypothesized type of matter that does not interact with “ordinary” matter except only gravitationally. This generation of this DM is not well-accounted for in the Standard Model Lagrangian (SML). The prevailing assumption that the early universe had equal amounts of matter and anti-matter requires that the symmetries of the SML be broken in ways such that: the net change in the baryon number of an interaction is not 0 ($\Delta B \neq 0$ - Baryon number violation); that the interactions of left-handed particles and right-handed particles not be the same (violations of C- and CP-Symmetry); and that these interactions take place out of thermal equilibrium (lest any net change be undone). While violations of C- and CP-symmetry are required for explaining why anti-matter is so scarce in the universe today (existing only in extreme conditions such as accelerators or from interactions of such as cosmic rays), expounding on those points is beyond the scope of this thesis.

1.2 Mirror Matter as an Explanation

1.2.1 Dark Matter, Mirror Matter, and Mirror Neutrons

Galactic cluster energies as determined via the virial theorem [36], the rotation curves of galaxies [30], gravitational lensing surveys [18], and evidence from Cosmic Microwave Background Radiation surveys (e.g., WMAP) all provide convincing evidence for the existence of a phenomenon commonly attributed to dark matter (DM). While its exact nature is not understood, the effects are clearly seen in a number of disparate aspects of astronomy and cosmology.

One candidate theory for the explanation of dark matter is "Mirror Matter" (MM) [6, 11]. A counterpart of ordinary matter (called the "mirror sector") with the same quantum numbers as in the SM but not interacting with the forces of the SM, mirror matter would require only a simple copy of the SM into its own sector (SM'). That is, corresponding to the $SU(3)_C \times SU(2)_L \times U(1)_Y$ form of the SM, there would be a corresponding $SU'(3)_C \times SU'(2)_L \times U'(1)_Y$ structure for the mirror sector. In either sector, the $SU(3)_C$ term is the group corresponding to the Strong nuclear components while the $SU(2)_L \times U(1)_Y$ corresponds to the Electroweak components. Coupling terms between the ordinary SM and the mirror SM' would introduce a new force that would allow for the detection of mirror matter via indirect observation due to transformation from ordinary matter into mirror matter.

Accordingly, mirror matter would then imply the existence of mirror particles such as mirror protons, mirror neutrons (n'), mirror photons, mirror electrons, and mirror neutrinos as well as the corresponding forces that act upon these mirror particles (but that do not act upon the ordinary matter versions of these). All properties of mirror neutrons in the SM' would be the same as those of the ordinary neutron, though some differences are possible. Due to the breaking of mirror symmetry at high energy scales, a non-degenerate mass of the n' is possible:

$$\Delta m = m_{n'} - m_n \neq 0. \tag{1.1}$$

Another possible new physical quantity is a small neutron transition magnetic moment (nTMM) arising as an electromagnetic correction in both the ordinary and mirror sectors due to the existence of the $n \to n'$ transition. **Figure 1.1** contains an example diagram depicting the process of a neutron transforming into a mirror neutron.

1.2.2 Mirror Neutrons

The transformation between matter and mirror matter is permitted only for neutral particles as the conservation of charge precludes charged particles from transforming into their mirror counterparts. Thus, only the neutral particles could be used as instruments for probing this hypothesis. Since most neutral particles are either so elusive so as to be impractical, such as neutrinos, or too difficult to produce and too short lived to be of use (such as the π^0), neutrons are the most obvious choice of particle. They are neutral, stable in nuclei, and are the longest-lived particle, with free neutrons having a half-life of ∼10 minutes. Neutrons usually decay into a proton, electron, and anti-electron neutrino via the Weak force (so-called "beta decay", named after the emitted β particle, the electron). Further, neutrons are also easily produced in large amounts at spallation sources or in nuclear reactors, meaning probing for suppressed, higher-order Lagrangian terms is feasible.

Using neutrons then means looking for the signature of a mirror neutron transformation. Such a transformation appears as either a neutron disappearing from where it would be expected to be found, a neutron appearing from where one is not expected, or the combination of both. As this is a suppressed interaction, considerable effort is needed in order for a statistically significant number of neutrons transformations to be detected, meaning the appearance of a neutron without the disappearance is not a practical experiment. However, the combination of a disappearance combined with (re)appearance is feasible. These experiments are called "regeneration" experiments.

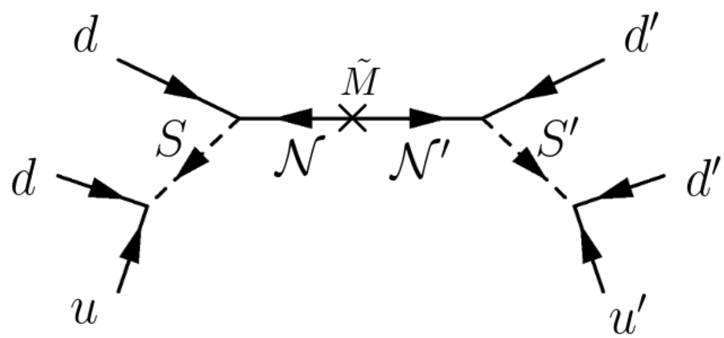

Figure 1.1: An example of a possible mechanism for the oscillation of matter into mirror matter. Figure 1 of [6].

While this type of experiment has been proposed and used in kaon-based experiments (such as in CP-Violation searches [16] and axion ”shining-through-a-wall” experiments [27], it is likewise well-suited for searching for the small effect the transformation mirror neutron mixing would present. The main thrust of these types of experiments is that the target particles can be induced to transform into a correlated particle (e.g., a sterile photon or mirror neutron) and pass through a barrier before transforming back into the original type of particle on the other side of the barrier, and that this transformation can be induced. Those particles that do not transform are removed by the barrier (a “thick” wall such as a neutron absorber), leaving only those particles that did transform (and transform back) to be detected. Specifically for mirror neutrons, model-dependent interactions can be exploited in order to further enhance the probabilities of transformation such as via the Landau-Zener effect. Such exploitation can reduce the difficulty of investigation by easing the requirements on the experiment.

1.3 Hamiltonian of the Transformation

It is the energy difference between two states in a system that permits the transformation between one state and another. In the case of mirror matter, there may be a number of underlying reasons for the differences, but the important aspect is that the neutron state and the mirror neutron state experience different potentials.

From Rabi oscillations in quantum mechanics, the Hamiltonian of the two-level n and n' system in the frame of the particle is

$$H = \begin{pmatrix} H_n & \epsilon \\ \epsilon & H_{n'} \end{pmatrix} \tag{1.2}$$

where

$$H_n = m_n + \mu_n(\vec{\sigma} \cdot \vec{B}_n) + V_n - iW_n$$
$$H_{n'} = m_{n'} + \mu_{n'}(\vec{\sigma} \cdot \vec{B}_{n'}) + V_{n'} - iW_{n'}$$

In the above, $H_{n,n'}$ is the energy of the (mirror) neutron, $m_{n,n'}$ is its mass, $\mu_{n,n'}$ is the magnetic moment of the particle, $\vec{B}_{n,n'}$ is the magnetic field present, $V_{n,n'}$ the real part of the optical potential of any medium the particle is traveling through, $W_{n,n'}$ is the imaginary part of the same, and ϵ is the model-dependent mixing term that may include dependence on quantities such as the magnetic field or an ambient magnetic vector potential field.

Subtracting the constant terms from the diagonal of the Hamiltonian in Equation (1.2) and assuming that the presence of either a mirror magnetic field or mirror material in an Earth-based laboratory is negligible, the simplified form can be obtained:

$$H = \begin{pmatrix} V - \Delta m \pm \mu B - iW & \varepsilon \\ \varepsilon & 0 \end{pmatrix} \tag{1.3}$$

where $\Delta m = m_{n'} - m_n$, $|\vec{B}_{n'}| = 0$, $V_{n'} = 0$, and $W_{n'} = 0$. The primary focus of the work detailed in this thesis is on the model put forth primarily by Berezhiani, though the last chapter details an external analysis of an experiment whose analysis was based on a string theory formulation of the transformation.

1.4 Berezhiani's Formulation

In the Berezhiani formulation, the general Hamiltonian of the transformation appears as

$$H = \begin{pmatrix} V - \Delta m \pm \mu B - iW & \varepsilon + (\eta \vec{B}_n + \eta' \vec{B}_{n'}) \cdot \sigma \\ \varepsilon + (\eta \vec{B}_n + \eta' \vec{B}_{n'}) \cdot \sigma & 0 \end{pmatrix} \tag{1.4}$$

where ε is the interaction strength of the force that transforms neutrons into mirror neutrons (and vice versa) and η & η' are the "neutron transition magnetic moment" (nTMM), a magnetic moment the particle would feel from the opposite sector's magnetic field. It is not known what the strength the mirror magnetic field $\vec{B'}_{n'}$ could have, but it is commonly assumed that is negligibly small and is often set as 0 [5] in calculations. This leaves three different parameters for experiments to investigate: Δm (the mass difference between states), ε (the strength of the mixing of matter and mirror matter), and η (the "amount" of the other sector's field the particle "feels").

While the methods for investigating the Δm and the η models are not mutually exclusive, Δm is expected to be on the order of $\mathcal{O}(100\text{ neV})$ [5] while there is no previously-computed expected value for η. In order to more clearly identify the possible effects of each model, the two models are investigated separately. Most of the work involved in this thesis is in the investigation of the $\Delta m \neq 0$ model, so while the $\eta-$type will be described briefly in §1.4.3 and a related future experiment is mentioned therein, in this work there is no experiment investigating it.

1.4.1 Observed Probability, ε, and The Mixing Angle θ

Though not the original source of the model, the relevant-to-experiment theory for the Δm model can be found in reference [20]. The derivations of the equations that follow are all contained therein and will not be reproduced here. However, a paraphrase of the relevant points of that paper is produced here in order to prepare for the chapters on the SNS and HFIR experiments.

The Hamiltonian for the Berezhiani formulation,

$$\mathcal{H} = \begin{pmatrix} U - iW & \epsilon \\ \epsilon & 0 \end{pmatrix} \tag{1.5}$$

where U is the real part of the potentials felt by the neutron (e.g., V, $\mu_n \vec{B} \cdot \vec{\sigma}$) and W is the imaginary part (W_{abs}, Γ_n). That this Hamiltonian is clearly non-Hermitian does not preclude diagonalization via canonical transformation:

$$S\mathcal{H}S^{-1} = \mathcal{H}_{diag} = \text{diag}(H_1, H_2) \equiv \mathcal{H} = S^{-1}\mathcal{H}_{diag}S. \tag{1.6}$$

Taking S as non-singular and with determinant 1:

$$S = \begin{pmatrix} c & s \\ -s & c \end{pmatrix}, \quad c = \cos\zeta, \quad s = \sin\zeta \tag{1.7}$$

with

$$\tan(2\zeta) = \frac{2\epsilon}{U - iW}. \tag{1.8}$$

As a result of the non-Hermiticity of Equation (1.5), $\zeta = \theta + i\omega$ (θ being the mixing angle between states and ω being the oscillation frequency between the states) and the eigenvalues $H_{1,2}$ are generally complex-valued. As the canonical transformation in (1.6) preserves the trance and determinant of $\mathcal{H}$, the traces and the determinants of the two matrices must remain equal. To wit: $H_1 + H_2 = U - iW$ and $H_1 H_2 = -\epsilon^2$. Thus:

$$H_{1,2} = U_{1,2} - iW_{1,2} = \frac{1}{2}\left(U - iW \pm \sqrt{(U - iW)^2 + 4\epsilon^2}\right). \tag{1.9}$$

Thus, the solution to the Schrödinger equation ($i\frac{d}{dt}|\Psi\rangle = \mathcal{H}|\Psi\rangle$) in a constant medium is then

$$|\Psi(t)\rangle = \mathcal{S}(t)|\Psi(0)\rangle, \quad \mathcal{S}(t) = \exp(-i\mathcal{H}t) = S^{-1}\text{diag}\left(\exp(-iH_1t), \exp(-iH_2t)\right)S. \tag{1.10}$$

The transition probabilities are then contained in the evolution matrix $\mathcal{S}(t)$:

$$\mathcal{S}(t) = \begin{pmatrix} \mathcal{S}_{nn}(t) & \mathcal{S}_{nn'} \\ \mathcal{S}_{n'n}(t) & \mathcal{S}_{n'n'} \end{pmatrix} = \begin{pmatrix} c^2e^{-iH_1t} + s^2e^{-iH_2t} & cs\left(e^{-iH_1t} - e^{-iH_2t}\right) \\ cs\left(e^{-iH_1t} - e^{-iH_2t}\right) & s^2e^{-iH_1t} + c^2e^{-iH_2t} \end{pmatrix}. \tag{1.11}$$

Starting with a pure neutron state $|\Psi(0)\rangle = |n\rangle = (1,0)^T$, the probability of finding the desired state is the square of the corresponding matrix element of the evolution matrix. The interesting quantities are $P_{nn}(t)$ and $P_{nn'}(t)$, the probabilities that the system will be measured as a neutron after starting as a neutron, and the probability that it will be measured as a mirror neutron after starting as a neutron. The limitation of the above solution, while analytic for the given assumptions, is that it only applies for constant potentials: constant material and a constant magnetic field value. The implementation of this solution into a practical calculation will be detailed later in §3.5.

1.4.2 Δm and θ

In this model, the neutron and mirror neutron have different masses while $\eta = \eta' = 0$, meaning that the oscillation between the two states is driven by this energy difference in the masses. For this model, the relevant form of the Hamiltonian for this model is

$$H = \begin{pmatrix} V - \Delta m + \mu B - iW & \varepsilon \\ \varepsilon & 0 \end{pmatrix}. \tag{1.12}$$

The probability for a given time t that a particle is in the neutron or mirror neutron state can be calculated calculated from the $|\mathcal{S}_{nn}(t)|^2$ and $|\mathcal{S}_{nn'}(t)|$ terms:

$$\begin{aligned} P_{nn}(t) &= |c|^4 e^{-wW_1 t} + |s|^4 e^{-2W_2 t} + 2\mathrm{Re}(c^{*2} s^2 e^{i\Delta E t})e^{-Wt} \\ P_{nn'}(t) &= \frac{1}{4}|\sin(2\zeta)|^2 \left[e^{-2W_1 t} + e^{-2W_2 t} - 2\cos(\Delta E t)e^{-Wt}\right] \end{aligned} \tag{1.13}$$

where $\Delta E := U_1 - U_2$ is the difference between the real part of the energies of the neutron and mirror neutron states.

1.4.3 η and θ

An alternative version of the MM model (but one not in opposition) instead supposes that the two sectors have the same higgs VEV removing any mass differences. Instead, the instigation of the transformation comes from a shared magnetic moment between the two states - that the neutron has some non-zero sensitivity to mirror magnetic fields (the coupling term η) and conversely that the mirror neutron has some sensitivity to ordinary magnetic fields (the coupling term η'). The parameter θ is the same in this case as it was in the $\Delta m-$based model - the mixing between the two states

- but the parameter η describes the contribution of the opposite sector's magnetic field to the particular particle. This theory, while not relevant to this thesis beyond being an alternative and related test of mirror matter theories, is the basis of the upcoming 2025 experiment at the HFIR that seeks to exploit these couplings in order to test for an effect.

1.4.4 Improving Transformation Probability via Landau-Zener Transitions

In either the Δm or η models above, the transformation can be enhanced through a Landau-Zener transition. While it is possible for a neutron to be measured at any given time to be in the neutron (or "missed" from being in the mirror neutron state), the probability of the transformation can be greatly enhanced by compensating the suppressing factors from material contributions as well as model-dependent factors (i.e., mass).

For example, in the Δm model, equation 1.8 appears as

$$\tan(2(\theta + i\omega))) = \frac{2\epsilon}{V_F - \Delta m + \mu B - iW}. \tag{1.14}$$

Maximizing the effect occurs when $W = 0$ and $\mu B = V_F - \Delta m$, meaning $2\theta = 90°$ and $\omega = 0$. Then, $P_{nn'}$ of 1.13 simplifies to

$$P_{nn'}(t) = \sin^2(2\theta)\left[1 - cos(\Delta E t)\right] = \frac{4\varepsilon^2}{\Delta E^2}\sin^2\left(\frac{\Delta E}{2}t\right) \tag{1.15}$$

with $P_{nn} = 1 - P_{nn'}(t)$ as expected by unitarity.

1.5 String Theory Formulation

An alternative formulation is based on String theory's brane cosmology [32]. In this type of theory, it is the physical separation of the multidimensional branes, δ, that is the impetus for the neutron's transformation into a mirror neutron while the difference in in-brane energies (energies due to the various potentials a neutron feels) corresponds to a mass difference term like the one introduced in Equation (1.1). See **Figure 1.2** for a depiction.

1.5.1 Phenomenology Following The String-Theory Model

As described in [26, 32] and references 12 - 14 in [26], the dynamics of a free neutron in electromagnetic and gravitational fields is described by

$$i\hbar \frac{\partial}{\partial t} \begin{pmatrix} \psi_+ \\ \psi_- \end{pmatrix} = (\mathbf{H}_0 + \mathbf{H}_{cm}) \begin{pmatrix} \psi_+ \\ \psi_- \end{pmatrix} \tag{1.16}$$

where the $\pm$ identify which brane's wave function the (otherwise-usual) Pauli spinors $\psi_\pm$ correspond to.

The Hamiltonian $\mathbf{H}_0$ is block diagonal and is the nonrelativistic evolution of two uncoupled spin -1/2 fields in the magnetic fields $\mathbf{B}_\pm$ and gravitational potentials $V_{\pm}$:

$$\mathbf{H}_0 = \begin{pmatrix} \mathbf{H}_+ & 0 \\ 0 & \mathbf{H}_- \end{pmatrix} \tag{1.17}$$

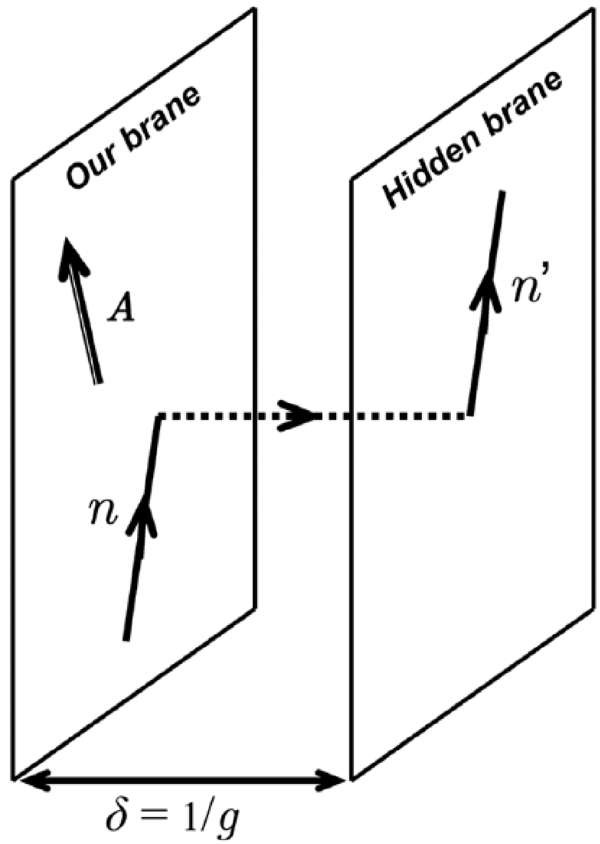

Figure 1.2: A "[n]aive view of the neutron swapping between two branes." Here, **A** is the ambient magnetic vector potential influencing the transformation while δ is the "effective distance between each brane" and g is the coupling strength of the branes [32].

where

$$\mathbf{H}_{\pm} = -\frac{\hbar^2}{2m}\Delta - \mu_n \sigma \cdot B_{\pm} + V_{\pm}, \tag{1.18}$$

m is the mass of the neutron, μ_n is the magnetic moment of the neutron, and Δ is the Laplace operator. The $\mathbf{H}_c m$ is the non-diagonal part of the Hamiltonian and describes the coupling between the branes:

$$\mathbf{H}_c m = g\mu_n \begin{pmatrix} 0 & -i\sigma \cdot \{\mathbf{A}_+ - \mathbf{A}_-\} \\ i\sigma \cdot \{\mathbf{A}_+ - \mathbf{A}_-\} & 0 \end{pmatrix} \tag{1.19}$$

where the $\mathbf{A}_{\pm}$ correspond to the magnetic vector potentials in their respective branes.

Chapter 2

Overview of Experiments

2.1 Neutron Regeneration Experiments

As the mirror neutron itself is invisible to detectors, experiments must rely on indirect observations for evidence that a mirror neutron was involved. To this end, “regeneration” experiments are used, experiments in which conditions are established in which the target particle is allowed to be removed from the system (either such as by decay or by capture) before the daughter particles “regenerate” the target particle. Such an experiment was used in [16] to identify the presence of K_S mesons (the short-lived superposition of the kaon states K^0 and $\bar{K}^0$ with quark content $\frac{d\bar{s}-s\bar{d}}{\sqrt{2}}$) or in the proposed mirror matter experiment of Gninenko and Krasnikov using neutral kaon beams [13]. Regeneration experiments are set up in such a way so as to detect particles that would have otherwise been removed from a system. For example in the Good et al. experiment [16], a neutral beam of kaons traveled far enough for a significant portion of the short-lived states to decay. After, the beam was impinged upon a matter target (in this case a liquid hydrogen target) whereupon a detector (a propane bubble chamber) downstream was able to detect the presence of short-lived species once again when there should have been statistically none. Depending on the "opacity" and purpose of the matter target (i.e., as an absorber or dump instead of a target meant to produce a desired reaction), such experiments can also be referred to as "X shining through walls" experiments where X is the desired signal particle heralding the effect, often as light, such as in CERN's OSQAR experiment [27].

2.2 Overview of Current Experiments

The experiments detailed later in this work are by far not the first experiments searching for mirror matter. Ultra-Cold Neutrons (UCNs - those neutrons that can reflected under any angle of incidence but have a velocity of ~7 m/s), prior experiments at the SNS, and experiments using neutrino detectors have all been used to investigate the parameter space in hopes of finding a "positive" detection signal.

2.2.1 PRL

Reference [8] is the collaboration's first published experiment on the search for this effect. Performed at the SNS in July and August of 2019 at the 4A beamline. This experiment utilized 32 mm of B_4C as a neutron absorber in the center of a 2.5 T and a 5 T magnetic field (of both "spin-up" and "spin-down" polarizations) in order to search for an effect that would be caused by the magnetic field compensating for the various terms contributing to the energy difference between the neutron and mirror neutron states (see Eqn. 1.12). This experiment was able to exclude the possibility that the discrepancy in lifetimes reported between the "beam" experiments and the "bottle" experiments is *not* due to the transformation from neutrons to mirror neutrons in the beam experiments. The configurations of the experiments in Chapters 3 and 4 are almost identical to this one.

2.2.2 UCNs

In contrast to experiments that utilize a beam of neutrons, such as [8], ultra-cold neutron (UCN) experiments such as [14] and [23] use a specially designed array of magnets to trap neutrons, a "bottle". The experiments in [14, 23] were specifically designed for investigating the neutron lifetime as it is useful for determining the value of the Cabibbo-Kobayashi-Maskawa matrix element V_{ud} as well as ^{4}He abundances (see, e.g., Reference [9]) which are important for cosmological models.

UCN experiments deal in neutron kinetic energies that are comparable to the optical potentials (from the Strong force) of the materials used in the experiments, on the order of $\mathcal{O}(100)$ neV. Understanding the losses due to absorption (such as on walls or coatings) and concerns of the adiabaticity of controlling the states of neutrons are of key import for being able to quantify systematic errors. The requirement of the highly-quantified errors means that these types of experiments are well-suited for looking for the effect of systematic disappearance or regeneration of neutrons.

2.2.3 STEREO

A regeneration experiment that substitutes neutrons and mirror neutrons for neutrinos and sterile neutrinos, the STEREO experiment was a neutrino detector that was placed at the High Flux Reactor (RHF) of the Institut Laue-Langevin in Grenoble, France originally to determine the nature of the reactor (anti-electron) neutrino defect [2]. An upgrade in every way to a related experiment [35], the collaboration was able to take numerous reactor cycles' worth of data and publish a limit on the $n \to n'$ transformation.

Chapter 3

SNS 2020

3.1 Spallation Sources

It is common knowledge that a nuclear fission reaction, such as from the decay of uranium-235, releases a number of neutrons. While some of these neutrons are required to sustain the reaction, others are able to be used for experiments. For example, in the case of the decay of U-235, 2.5 neutrons are released on average per decay event. One neutron is required to sustain the chain reaction, leaving 1.5 neutrons available for experiments. However, fission is not the only method for producing neutrons available for experiment. A spallation source is able to produce up to 10 times as many neutrons free for experiment than a reactor is able to for a given mount of energy produced in the reaction that frees the neutrons [22]. That is, for every 1 MW of beam power in a spallation source, the same number of neutrons is produced as in a nuclear running at 10 MW_{th}. A spallation source is able to do this through the collision of two atoms, usually a hydrogen atom onto some much-heavier target atom such as tungsten or mercury, and directing the neutrons towards the experiments down the line. While the total flux (read: intensity of neutron beams) is currently higher in reactor-based facilities such as the HFIR, the controlled properties of a spallation beam mean more metadata is available for identifying the experiment beam's properties such as intensity or the variance in such. The greater understanding of these uncertainties afforded by the nature of a spallation source leads to a better understanding of the systematics of the experiment, a better understanding of the experiment result.

3.2 4A Beamline at the SNS

The 4A beamline of the SNS facility was used for a regeneration experiment in early November of 2020. **Figure 3.1** has the schematic of the experiment. The detector located at the beamline, the Magnetism Reflectometer (MagRef) has neutron detection capabilities for wavelengths as large as ~14 Å (corresponding to a neutron velocity of ~282.6 m/s) and as small as ~1.8 Å (~2198 m/s) [24]. However, the beamline has installed a velocity selection mechanism to limit the neutron wavelengths to between 1.8 Åand 5 Å, corresponding to velocities between 2198 m/s and 791 m/s but peaking at around 2 Å. **Figure 3.2** is a plot of the specific neutron wavelength spectrum that was received at the detector. In theory, the inclusion of the colder, slower neutrons would greatly improve the sensitivity to the “signal” of the effect (the unaccounted for neutron appearance in the detector), but low number of neutrons in the distribution’s tail would also mean the “noise” from the background would overpower any gain in sensitivity.

3.3 Beam Intensity Analysis

The 4A beamline of the SNS did not include any detectors along the beam to measure the number of neutrons passing through. For this reason, the number of neutrons passing through the experiment needed to be extrapolated using information provided from the DAQ systems and simulations from the Particle and Heavy Ion Transport code System (PHITS - [33]) over multiple calibration runs.

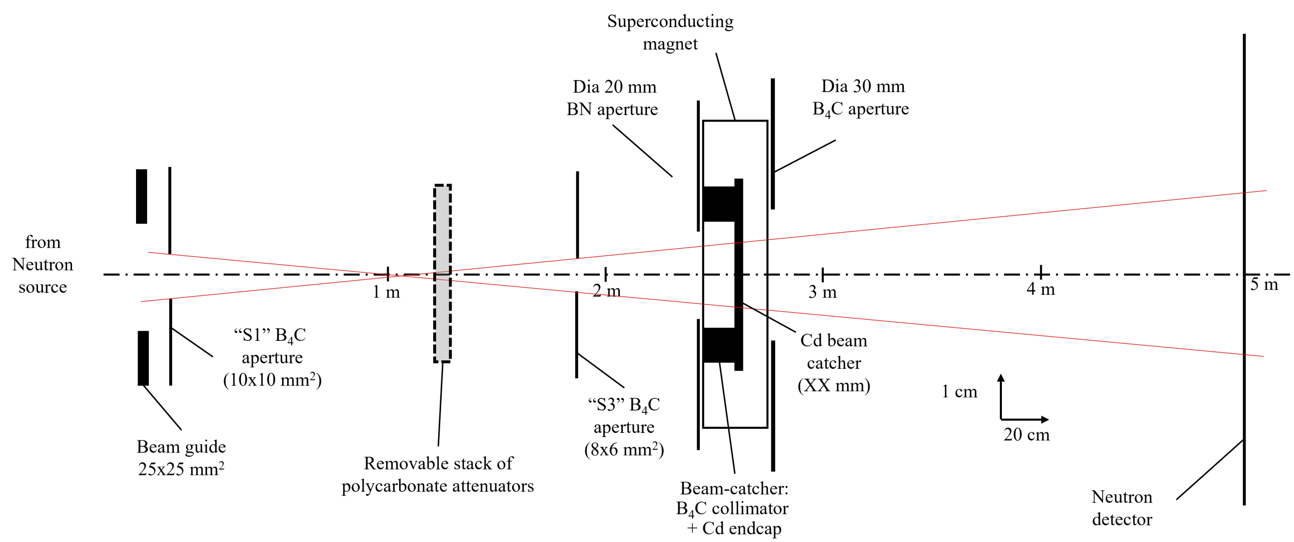

Figure 3.1: Figure 1 from [15]

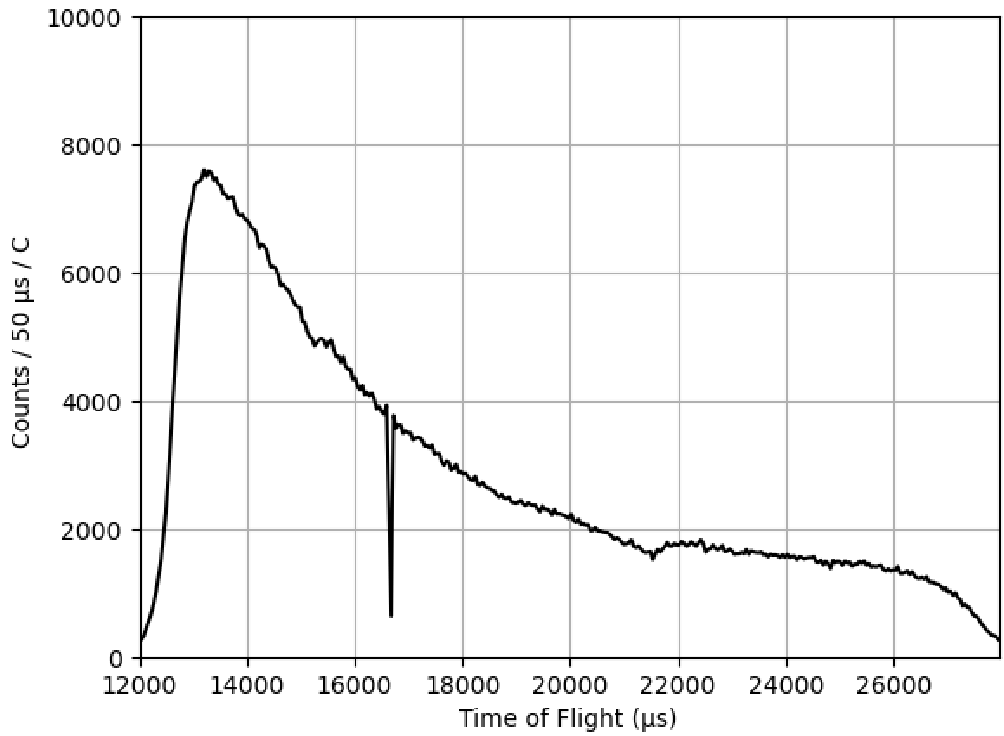

Figure 3.2: Figure 2 from [15] detailing the neutron spectrum in terms of binned detector counts versus neutron time of flight. The “cut” in the spectrum is a $\pm 50 \mu s$ window (100 μs wide) centered at 16,666 μs in order to exclude the “prompt flash”, the radiation emitted by the spallation source that can confound the analysis. In this figure, the 12000 µs counts correspond to a wavelength of 2.26 Å while the 26000 µs corresponds to a wavelength of 4.90 Å. The peak is ~15500 µs, ~2.92 Å.

These calibration runs utilized stacks of varying thicknesses of polycarbonate (nominally composed of chains of $H_{16}C_{15}O_2$) attenuators of a nominal thickness of 1.27 mm as the non-attenuated beam could cause damage to the detector. As the absorber used in the “normal operation” of the experiment, a piece of cadmium 3.5 mm thick, would absorb too many neutrons to be able to effectively determine the neutron beam’s initial intensity, these calibration runs used stacks of 18, 19, 20, 21, 22, and 24 plates duct-taped together into a stack to facilitate this process.

The initial intensity of the neutron beam at the 4A beamline was not known with sufficient precision for the purposes of the experiment to be performed. In order to quantify how many neutrons were in the beam initially, a set of simulations of the calibration runs were run through PHITS. As PHITS did not have the thermal scattering information for the hydrogen in polycarbonate, a material not chemically “well-defined” in the same sense that water or a metallic alloy could be considered “well-defined” in terms of a defined mixture or composition due to the various additives and incomplete processes in the manufacturing process, the thermal scattering kernel for the hydrogen in lucite (aka poly(methyl methacrylate)) from the Japanese Evaluated Nuclear Data Library version 5 (JENDL-5 - [19]) was substituted instead as the scattering behavior of the hydrogen in either polymer is different than for diatomic hydrogen gas (as would have otherwise been assumed for such scattering). The basis for choosing to use the hydrogen kernel of lucite was the assumption that the behavior for lucite would be more similar to that of polycarbonate than that of simple hydrogen.

These simulations used the known spectrum of the beamline as input as well as the materials placed in the beamline in order to get an approximate number of neutrons that should be seen at the detector. The materials and geometries in the simulations were meant to match as close as possible the reality of those in the beam, though substitutions due to technical limitations (i.e., treating the hydrogen in the PC as if it were in lucite instead) were present. As well, the expected number of neutrons for an unattenuated beam (i.e., no PC plates to attenuate) was also simulated in order to compare the extrapolated value to the directly-simulated value. Counting only those neutrons in the simulation results that remained unscattered, a fit over the simulations extrapolating back to the equivalent of "0 PC plates" was performed with a power law and compared to the direct simulation of the "0 PC" point. The fit over the experiment data skipped the value for the 21 PC point due to unknown factors conspiring and making that point an outlier (by measures of χ^2). For this reason, the simulation values also excluded the 21 PC point in the fitting. Finally, the ratio of the simulated 0PC point over the extrapolated 0PC value was found to be 1.254 ± 0.029. This correction comes from the increased interaction of the cold(er) neutron beam with the thermal polycarbonate plates. The final intensity value determined form the fit-to-experimental-data extrapolation were scaled up by these values and was computed as being $(3.215 \pm 0.121) \times 10^9$ counts/C. **Figure 3.3** has a plot of the residuals to this fit.

3.4 Background Analysis

In addition to any transformed neutrons, there are neutrons that are detected as part of the scattering from the PC background. These neutrons must be subtracted from the dataset in order to determine the number of regenerated neutrons. Multiple fitting models were tried in order to determine which best described the background seen in the detector, but a model with three free parameters for a plane in 3-D space (with coefficients b_0, b_x, b_y) and a Gaussian with two free parameters (amplitude A and x-width σ_x) was chosen. The value for the σ_y was chosen as a function $K\sigma_x$ with the scaling factor K taking the value of 1.05× larger. While this scaling value was slightly different between calibration runs, the difference was slight and the single value of 1.05 was used for all thicknesses of the PC attenuator. Excluding the search for the optimal scaling factor K, the process of fitting the different background models was repeated for all of the PC plate configurations used in the calibration runs.

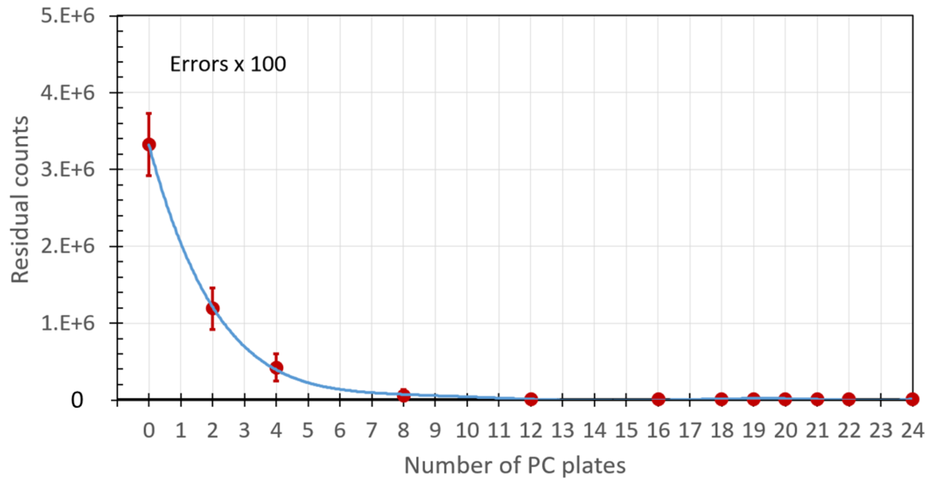

Figure 3.3: Residuals of the exponential fit from the results of the PHITS simulations, including the simulation-only conditions of 0, 2, 4, 8, 12, and 16 PC plates. The error bars have been magnified 100× for visibility. The increase in the residuals is due to the upscattering of the cold neutron beam from the room-temperature polycarbonate plates not being accounted for in the exponential fit.

A sample of the determination of the scaling factor K can be seen in **Figure 3.4** while the comparison of the σ_y/σ_x fitting χ^2 values is in **Figure 3.5**.

Once the background had been subtracted, the number of hits remaining in a particular region of interest were used as input to fit a two-parameter power-law (equivalent to an exponential), $F_0\eta^x$, where F_0 is the initial beam intensity extrapolated to 0 PC plates, η is the attenuation factor, and x is the number of PC plates (a re-scaling of the total thickness of plates).

After fitting and removing the contribution from the background (with an example histogram of the background fitting seen in **Figure 3.6**), **Table 3.1** contains the final regeneration probabilities per neutron and the corresponding confidence levels. These limits are plotted as dotted lines in the plots of **Figure 3.7**.

3.5 Simulation of Transition Probabilities

While the above sections §3.3 & §3.4 detail the determination of the initial intensity of the neutron beam, separate simulations using bespoke code written to leverage the parallelism of GPUs was used in order to determine the parameter space limits of our experiment. This code implemented the density matrix formulation of Ref. [21] via the CUDA library for Julia 1.6.7. The 2×2 matrix was rearranged into a 4×1 vector permitting the Hamiltonian that describes the time evolution of the system to be diagonalized via canonical transformation into the Jordan normal form.

The complex elements ρ_{12} and ρ_{21} were rewritten as a and b, the real and imaginary components of the density matrix, to simplify the GPU implementation. A V100 GPU of UT Knoxville's ISAAC-NG cluster was utilized for these simulations though testing and smaller-scale simulations were performed on personal hardware. Investigations into the optimization of parameters was also performed using the V100 as Nvidia's consumer-grade RTX GPUs have limited double-precision throughput compared to a commercial-grade Tesla accelerator's.

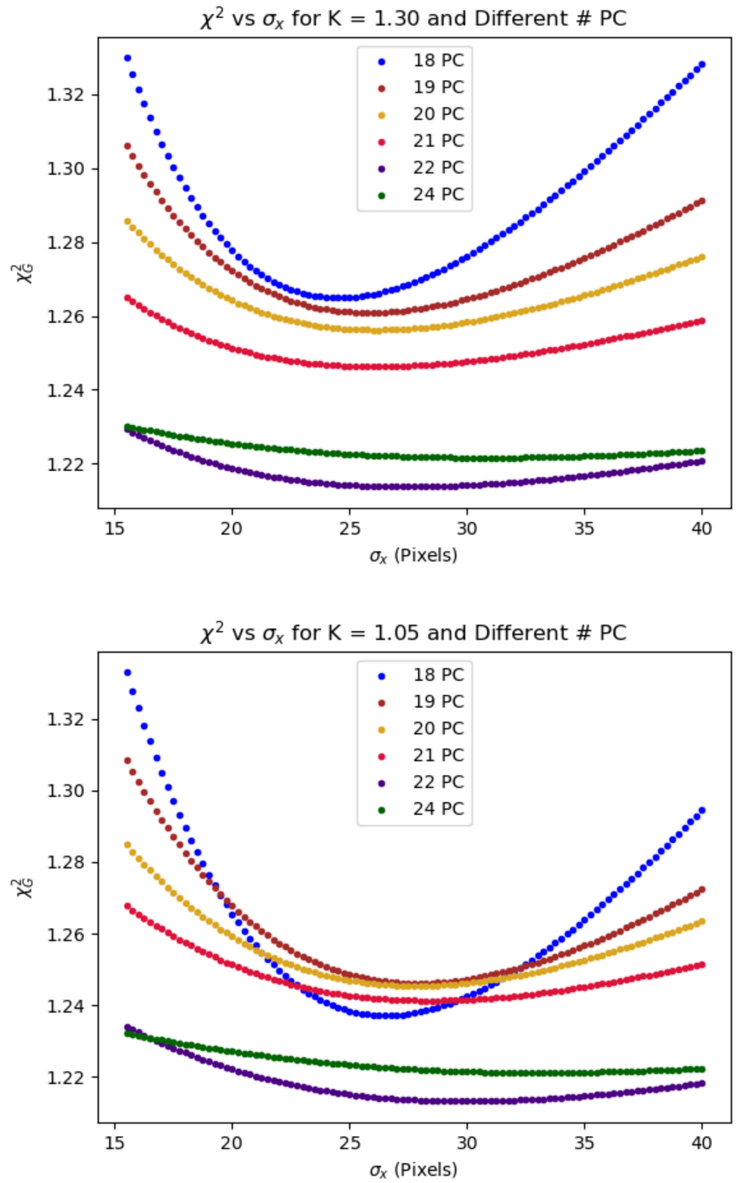

Figure 3.4: Two examples of varying the ratio $\frac{\sigma_y}{\sigma_x}$ to determine the optimal value for later fitting.

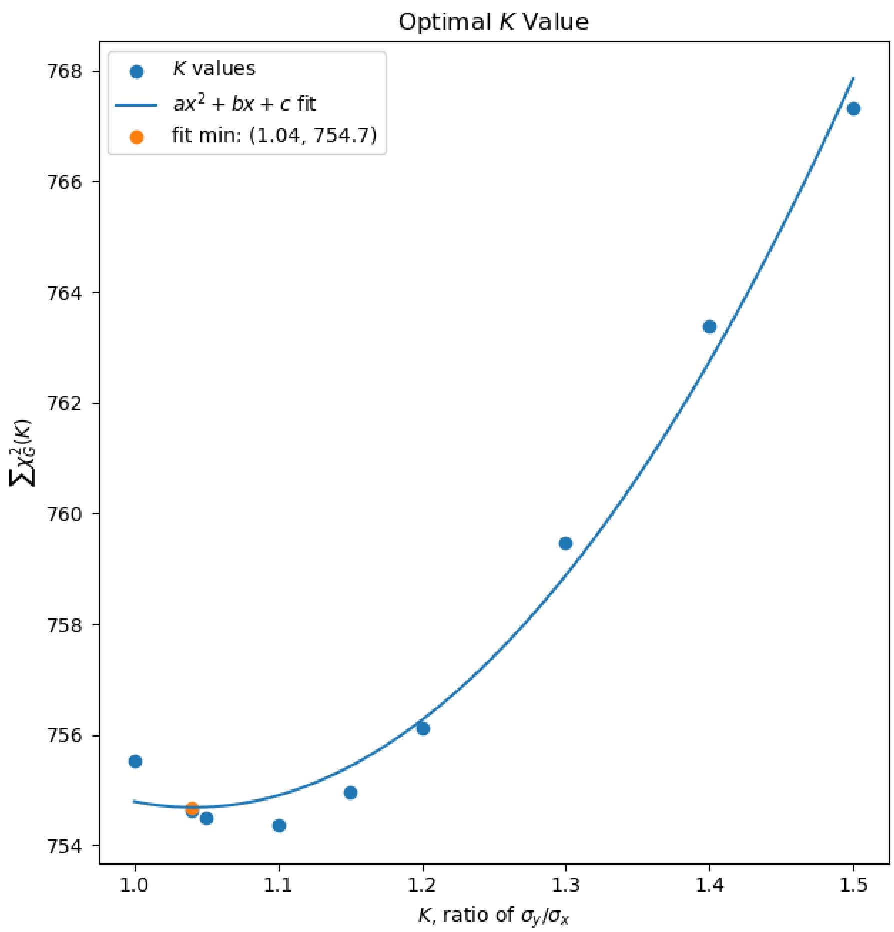

Figure 3.5: Examples of the effect of the different scaling factors on accounting for the background of different runs. The y-axis is the non-normalized χ^2 value for each fit. The x-axis is the value of the ratio of $\frac{\sigma_y}{\sigma_x}$. The values of the Gaussian's amplitude and the fitting plane's coefficients were fixed.

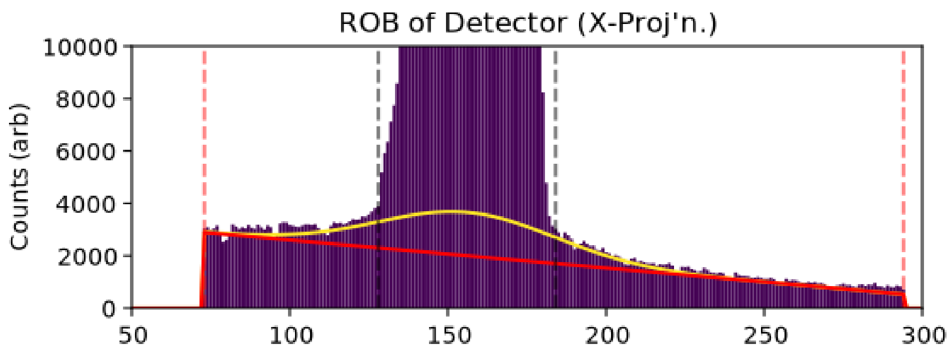

Figure 3.6: The projection onto the x-axis of the neutrons MagRef detected in the 18 PC-plate calibration run. The red dashed lines are the extreme edges of the whole considered region of the detector, while the inner black dashed lines are those corresponding to the interior limit of the fitting.

Table 3.1: Table II listing signals and C.L.s from [15]

B-Field (T)	Signal ($\times 10^{-10}$)	95% C.L. p_{tr} ($\times 10^{-10}$)
4.70	-3.9 ± 3.2	3.1
2.35	-2.1 ± 3.2	4.4
4.7 and 2.35	-3.1 ± 2.7	2.8

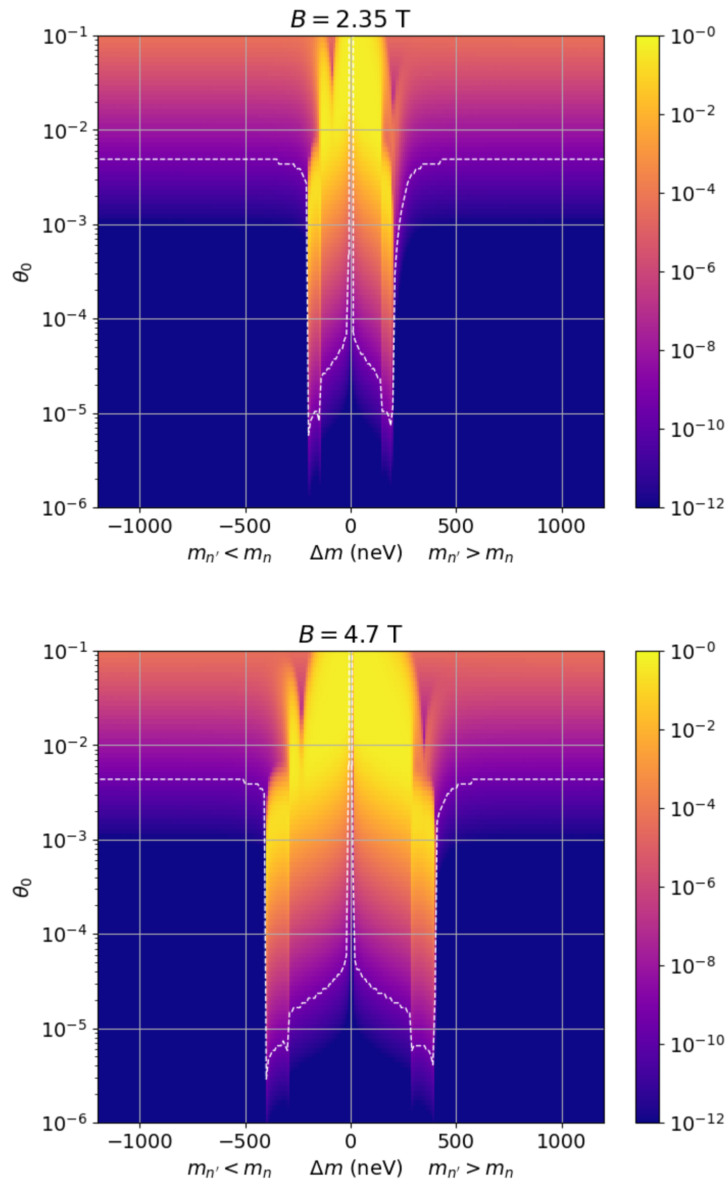

Figure 3.7: A "butterfly" plot, so called due to the color scheme and near-symmetric appearance. The white dashed line denotes the limit of our experiment's sensitivity for this magnetic field strength. The color scale to the right is a log scale of the probability of transformation, limited to 10^{-12}. Anything above the white line is excluded based on the lack of experimental observation for this magnetic field strength [15].

The result of these simulations for $m_{n'} > m_n$, $m_n > m_{n'}$, and $\pm|\vec{B}|$ were analyzed and stitched together to make a "butterfly" plot with a limit determined via Feldman-Cousins based on the experiment's observation data - see **Figure 3.7** for examples at nominal magnetic field values of 2.35 T and 4.7 T. The residual magnetization of the superconducting magnet (most likely from the iron yoke used in the construction of the magnet to constrain the field) is significant for the $|\vec{B}| = 0$ T runs. A constant residual field of ~3 mT was found in the magnet even after it was powered off. This was modeled as a $1/r^3$ field (due to the falling off of a dipole field as such) and used to model the sub-10 neV range of our simulations.

3.6 Final Results

All of the experiment runs yielded a result that was consistent with the null hypothesis ("no mirror matter"). These results translate to a probability of transformation per neutron no better than 2.1×10^{-10} (as seen in **Table 3.1**). An improvement of ~4× sensitivity was achieved over the PRL's by the reduction of the background that the detector sees (see the black curve in **Figure 3.8**). As can be seen, greatly-improved signal-to-background afforded a much clearer search through the parameter space. Notably, the "teeth" at ~200 neV and 300 neV which correspond to the two magnetic field magnitudes used are now plainly visible. Further, the use of a cadmium absorber instead of a B_4C absorber in the magnet removed the reduction in sensitivity in the 400 neV - 600 neV range that was due to the interaction of the complex optical potential of the B_4C and the 4.8 T magnetic field [8]. Other experiments, such as STEREO or UCNτ search for the same effect or can have their results translated into a search for the same. **Figure 3.9** compares the results of this experiment with a handful of others to show the "world parameter space" that has been excluded. Notably, it is the residual 3 mT field that provides this experiment with sensitivity in between that of UCN experiments and years-long running experiments such as STEREO or MURMUR.

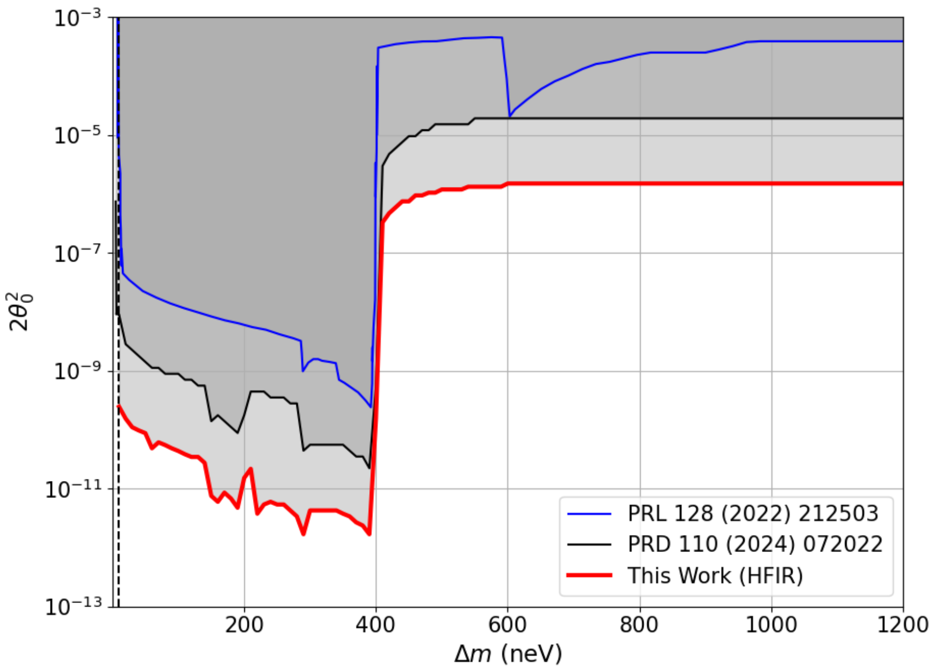

Figure 3.8: A comparison of the excluded regions of parameter space beyond the SNS experiment's sensitivities. As seen in the legend, the black curve traces the limit of these SNS 2020 experiment results while the red curve is the not-yet described HFIR 2024 results. The blue curve is of the experiment performed in 2019 and published in PRL in 2022.

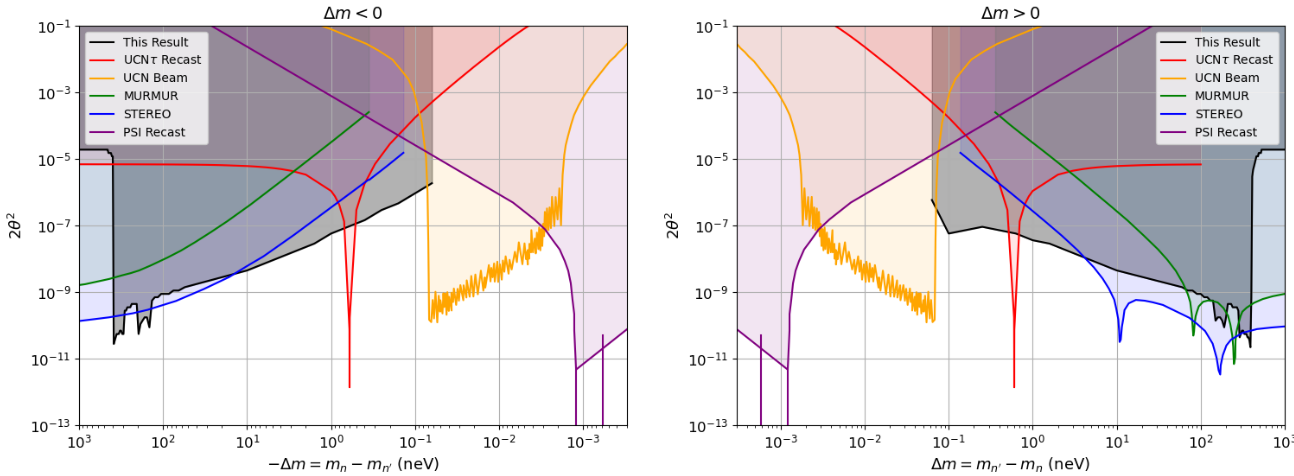

Figure 3.9: Comparison of these results to other experiments adapted from Figure 3 of Reference [4] - STEREO [3], MURMUR [35], UCNτ [14], PSI [23].

Chapter 4

HFIR 2024

In January of 2024, an experiment identical in concept to the one performed at the SNS in November of 2020 (Ch. 3) was performed at the HFIR. While it is true that spallation sources can produce neutrons with less downtime compared to reactors (e.g., for not having to shutdown handle fuel replacement) and with other favorable secondary characteristics (such as the pulsed nature of the beam impinging on the target) The choice of using the reactor as the neutron source in this experiment permitted a third magnetic intensity of 3.6 T to be used as the greater intensity in the beamlines allowed for the same sensitivity at a desired polarization in less time. Further, the Cold Guide Hall Beamline 2 (CG2) has monitoring appurtenances that the SNS experiment was not able to take advantage of. In contrast to the SNS experiment that required simulation in order to estimate the average beam intensity for the experiment, these monitors allow for directly measuring the beam.

4.1 Reactor As Source of Neutrons

While a spallation source can produce ~10x more neutrons than a fission reactor for a given amount of thermal energy released, there are still significant limitations. For example, the target of a spallation source must be able to dissipate the great thermal energy in a small area on the target due to the impinging of the charged beam as well as the spallation energies of the atoms of the target. This heat is not an insignificant challenge and fundamentally impacts the average neutron flux. A fission reactor can handle much higher thermal load meaning a much greater average neutron flux is available "downstream". To compare, the SNS has the approximate neutron flux of a 10 MW_{th} reactor while the HFIR is run at 85 MW_{th}. While the European Spallation Source will do much to bring the two types of sources into parity (and indeed is intended to replace the RHF at the ILL), it still stands today that a reactor can produce more neutrons for experiments.

The HFIR facility has a spectrum slightly lower than the SNS (compare **Fig. 4.1** to **Fig. 3.2**). This increase in the wavelength corresponds to an increase in the probability of transformation from neutron to mirror neutron (and back again). While the increase in the transformation probability is appreciated, the more meaningful aspect of the HFIR is the fact that the neutron flux is higher than at the SNS. It was expected that the flux would be ~100× greater, which was indeed seen at the detectors.

4.2 CG2 Beamline

The CG2 beamline is a series of eight removable aluminum vacuum guides, each 2 m in length and with built-in collimators (of boron carbide), windows between guides of 4 cm x 4 cm, and appurtenances for installing experiment devices such as motor units for possible movement (unnecessary for this experiment). This beamline is pumped down to a vacuum of ~10 mTorr (~1.333 Pa) via roughing pumps to minimize the number of particles (such as from the atmosphere) from which the neutrons can scatter from while in flight. These scattered neutrons tend to reduce the beam's intensity by being absorbed by the collimators of the vacuum guides so minimizing this scattering is valuable. As it is, due to a misalignment in the beam guides, approximately 25% of the beam's intensity is lost.

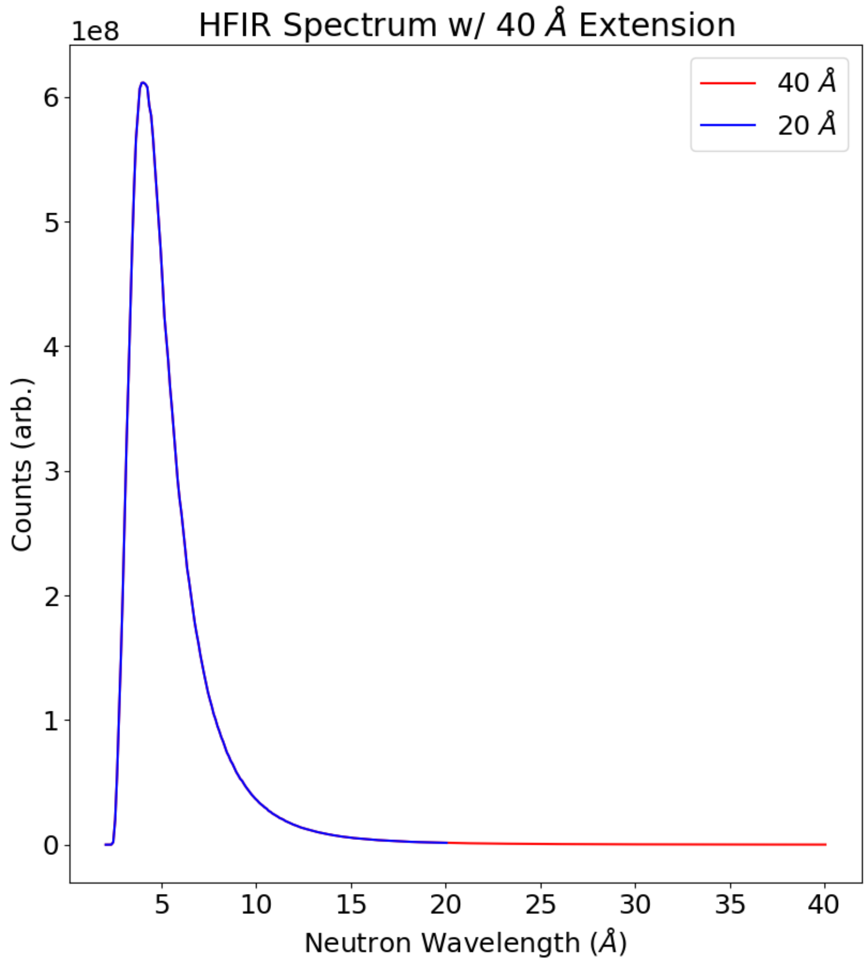

Figure 4.1: CG2 Beamline spectrum on natural scale. Spectrum data provided by staff scientist managing CG2 beamline. It was known that the neutron beam provided at CG2 has counts for wavelengths up to 40 Å but the number was not known. In blue is the spectrum up to 20 Å and in red is up to 40 Å. Normalization aside, the entirety of the SNS spectrum (from the time of flights measured) would fit in the region between the start of the plot and the 5 Å mark.

At the head of the vacuum guides is the "blue box", so called from the color of the casing, that houses an Ordella beam monitor (of stated efficiency 10^{-5}), the velocity selector unit and selection of attenuating lucite plates. The beam monitor's efficiency being so low means that it is practically invisible to the neutrons in the beam (removing ~0.001% of the beam) but still providing a measure of the intensity. The velocity selector unit is a cylinder with "teeth" on the inside coated in a neutron absorber. It is rotated at some rate in order to remove neutrons that do not fall within a window of velocities (or equivalently, desired wavelengths). This velocity selector was not used in our experiment and was removed from the beamline to provide it with "white beam", or, the whole spectrum from the reactor (that make it down to the guides from the neutron mirrors upstream). At the end of the vacuum guides is an extension ~1.3 m long with a window of sapphire 6.35 mm thick. This sapphire is to help remove short-wavelength neutrons from the beam as a form of conditioning.

There are eight positions for the attenuating slide in the "blue box" housing: one boron nitride beam blocker, six lucite attenuators, and one "open" position that has no attenuator which permits the full beam to pass through. These positions are labeled by their nominal attenuation rates. From the beam blocker (highest) to the lowest attenuator, they are: the boron nitride (BN) blocker, the 100k, the 10k, the 2k, 300, 30, 3, and the open position. Nominally, the 100k attenuator would reduce the beam intensity by a factor of 100k (or a multiplicative factor of 10^{-5}). However, the thicknesses of the attenuators listed on the as-built schematics do not correspond to these factors. **Table 4.1** has the nominal and actual attenuation factors provided by the attenuator positions. For this experiment, the “100k” attenuator was used for calibration purposes and the “open” position for the data-taking runs.

Table 4.1: Nominal and actual attenuation factors of the lucite blocks in the CG2 beamline along with the corresponding schematic and required thicknesses to reach the stated attenuation. Units of inches are listed here because the schematics are listed in inches.

Name	Nominal Attenuation Factor	Schematic Thickness (inches)	Actual Attenuation Factor	Required Thickness for Named Attenuation (inches)
100k	10^5	0.748	11780	0.9187
10k	10^4	0.630	2685	0.7349
2k	2000	0.512	612	0.6065
300	300	0.394	139	0.4551
30	30	0.236	19	0.2714
3	3	0.079	2.7	0.088

4.3 Beam Intensity Determination

Unlike the SNS BL-4A, the HFIR CG2 beam line had two possible beam monitors in place: one monitor fixed upstream in the "blue box" (referred to as the "GPM") and a second monitor that could be located slightly upstream or downstream of the superconducting magnet that is used to instigate the neutron-mirror neutron transformation. These monitors, both the GPM and those downstream by the magnet, are Ordella monitors calibrated to have an efficiency of 10^{-5}. While in the SNS experiment PHITS simulations were needed in order to determine the beam intensity, this HFIR experiment did not need such as these monitors were able to measure the (scaled) intensity. In order to determine the initial intensity of the beam, the readouts of the upstream monitor by the velocity selector and the second monitor in the position immediately upstream of the magnet were compared. As most of the beamline between the two monitors is a vacuum, the beam's initial intensity was determined by the upstream beam monitor (GPM) and the downstream Ordella monitor in place:

$$I_0 = \text{GPM} \times \frac{\text{GPM}}{\text{Ordella}}.$$

The average intensity of the beam for the runs data was taken was ~1.1×10^{10} neutrons/second.

4.4 Background Reduction

Unlike in the SNS experiment prior, the presence of a permanent beam monitor (the one in the upstream “blue box”) and only a single attenuator being used for calibration means that the process of accounting for the background is a much less involved process. A single run was used to specifically determine the shape and size of the beam spot on the detector. The cadmium plate was removed from the experiment while the 100k attenuator was put into position upstream as the naked beam on the detector could cause damage. The position of brightest spot was found using a simple algorithm checking the “interesting” regions of the detector the for maximum peak and recording its location. **Figure 4.2** has two such plots showing an interesting feature, “beam punchthrough” from the high-energy neutrons that remained in the beamline despite the facility’s attempts at removing them as well as a plot showing the intensity of the beam on the detector after it has passed through the attenuator. After the reduction of the background, a preliminary probability limit of 1.1×10^{-12} was determined as the threshold above which a signal would have been detected.

4.5 Simulation of Transition Probabilities

The CG2 beamline of the HFIR was very similar to that of the SNS’s BL-4A that the Ch. 3 took place in. A 3.5 mm cadmium plate was the neutron absorber put into place, the same model of superconducting magnet was used, and the only appreciable differences for the materials of the model was the inclusion of a sapphire window (0.5 inches in thickness) used in the beam to filter out shorter-wavelength neutrons, the silicon window of the GPSANS vacuum vessel (Miller indices of [111], 1 inch thick), and the vacuums of the beamline extension tube out of beam guide 8 and the GPSANS volume. The same magnetic field profile was assumed for both magnets. Technically this is incorrect as they are different magnet assemblies and should therefore have different field strengths due to the differences in their constructions, but such a file was not made available. The other appreciable difference in the simulation was the geometry of the simulation. The "region of simulation" for the Ch. 3 was approximately 600 mm in length: 300 mm upstream of the cadmium plate in the middle and 300 mm downstream of the cadmium plate. For this experiment, the region is approximately 3200 mm, approximately $5\frac{1}{3}\times$ the length of the SNS 2020 experiment.

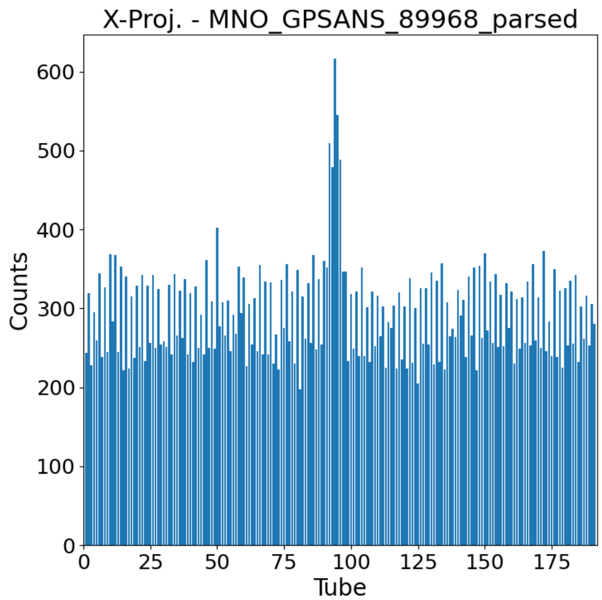

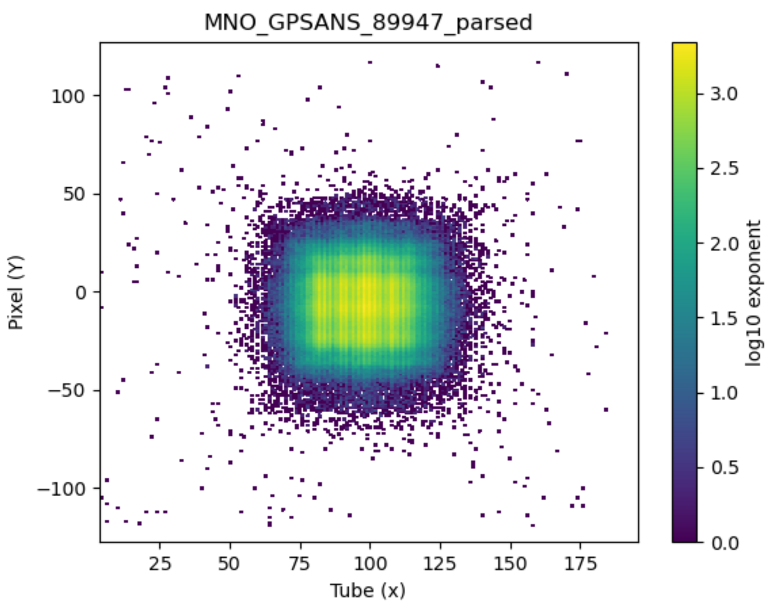

Figure 4.2: Sample outputs for the detector. **Top:** a projection of the data of run #89968 onto the x-axis to determine the location of the peak. **Bottom:** on a log scale, the hit pattern of run #89947 shows more the size of the spot that will be accounted for, though less information about the intensity and the location of the brightest part of the beam is available.

UT Knoxville's ISAAC-NG cluster's V100s are insufficient for the task of computing the probabilities through this increased trajectory as the increased time required would run afoul of the time limitations imposed on the number of parameters of Δm, θ_0 and the number of velocities sampled and an adaptive step size algorithm was not put in place for these calculations. For this reason, the H100s of Georgia Institute of Technology's PACE cluster were utilized for these computations. The plots of the calculation's output for the 2.4 T and 4.8 T magnetic field values are in **Figure 4.3** with the white dashed line corresponding to the improved limit.

4.6 Preliminary Results

Unfortunately there was no positive identification of regenerated neutrons. However, preliminary results indicate that a combined transformation limit of approximately ~1.1×10^{-12} is expected. **Figure 4.4** shows where these results from this experiment lie while **Figure 4.5** plots the improvement this experiment had over the previous one performed at the SNS. In the experiment detailed in **Ch. 3**, the improvement over the previous version of the same experiment, reference [8], was due to greatly-improved understanding and control of the backgrounds. In this experiment, the improvement comes from similar control of the backgrounds while maintaining a much higher neutron beam flux. It is this greatly-improved flux that drives the increase in the sensitivity. However, as there was no "detection" of a $n \to n' \to n$ signal and there is not a convenient neutron flux source with ~1000× the intensity of the HFIR, the next choice is to opt for an increased amount of beam time. This is not an option at the HFIR due to the nature of the facility (being a material science-focused facility and not primarily a fundamental research facility).

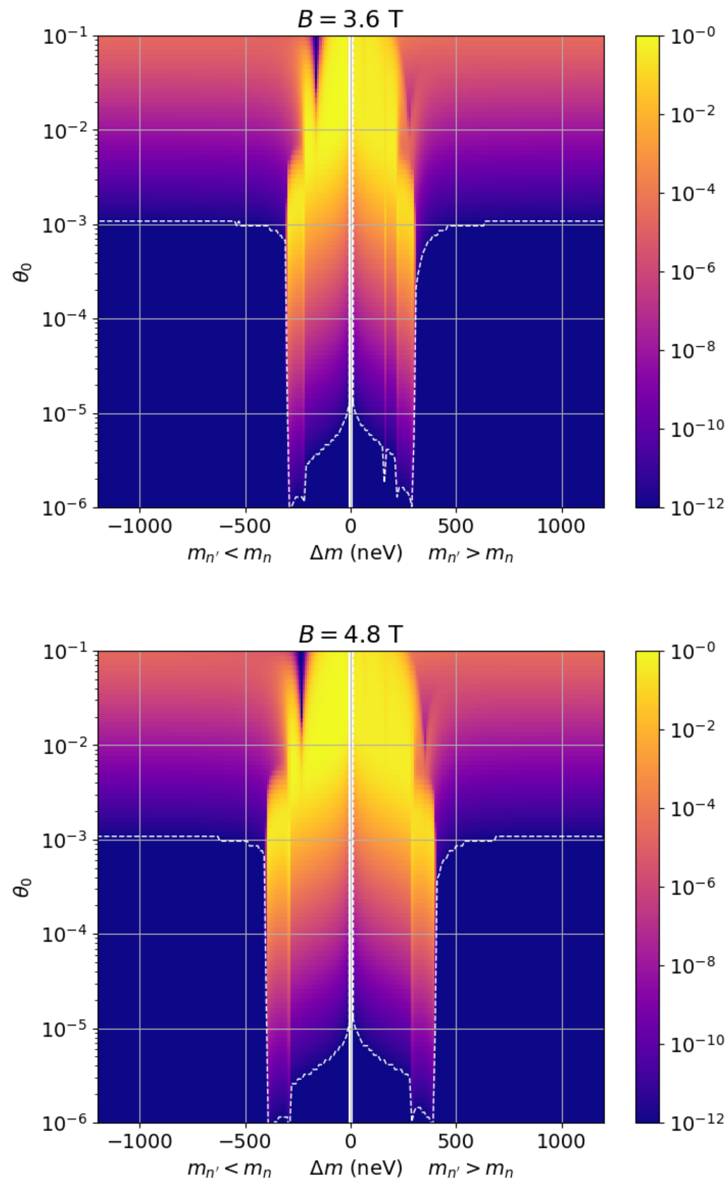

Figure 4.3: Butterfly plots of the 3.6 T and 4.8 T magnetization for the HFIR CG2 beamline geometry. The dashed white line traces out a probability limit of 1.1×10^{-2}.

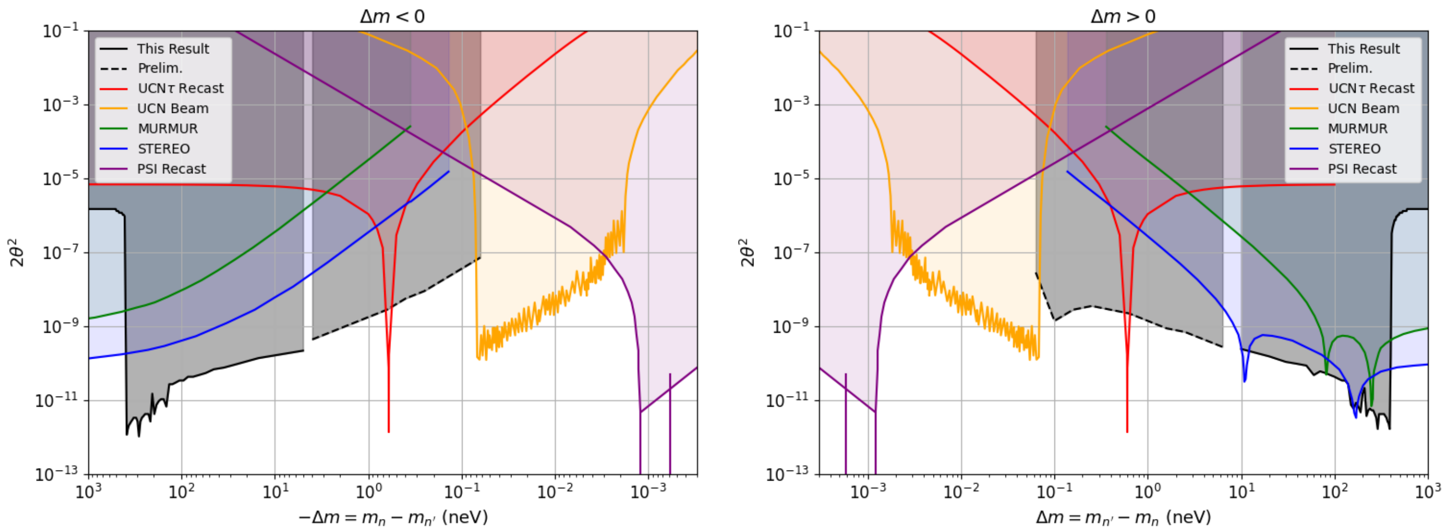

Figure 4.4: Fundamentally the same plot as **Figure 3.9** but with the results from the limit found from this experiment (the solid black line) combined with the simulations from the low-residual magnetic field values of the SNS 2020 experiment (the dashed black line).

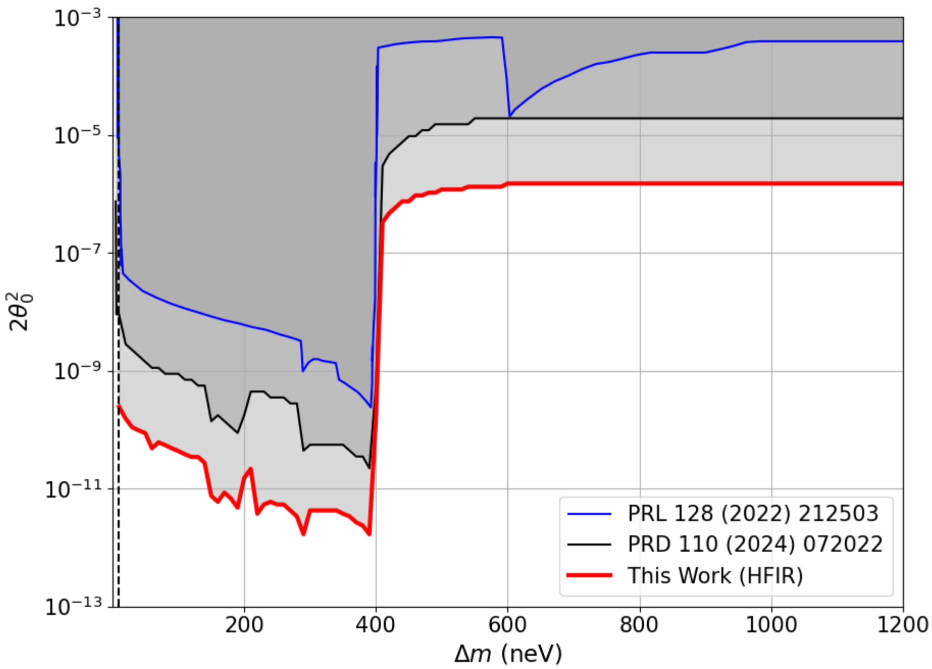

Figure 4.5: A comparison of the excluded regions of parameter space beyond the SNS experiment's sensitivities. As seen in the legend, the black curve traces the limit of the SNS 2020 experiment while the red curve is these results. The blue curve is of the experiment performed in 2019 and published in PRL in 2022.

Chapter 5

STEREO at the ILL

5.1 String Theoretic Formulation As Used by The STEREO Collaboration

Just as in the case of neutron-antineutron oscillations, the interactions of mirror matter with regular matter have also been formulated with a string-theoretic underpinning ([31] and others as well). Many of these theories rely on some notion of multiple branes interacting in a “bulk” where the interaction itself is the fundamental cause of the transformation between the two states. One particular such theory (cite Sarrazin’s papers on this) as proposed by Sarrazin was the basis of experiments performed using the MURMUR and STEREO detectors [3, 35]. While the mathematic details of Sarrazin et al.’s formulation are not pertinent to this dissertation, the most relevant consideration is that the interaction between the brane containing the mirror neutrons and our brane can be modeled as the interactions of an open quantum system. With this consideration, the Lindblad master equation is employed to handle the transformation between neutron and mirror neutron in this formulation.

5.2 Theory: Interactions in Open Quantum Systems Leading to Mirror Neutron Transformation

The interaction between particles constitutes a measurement. Upon measurement, a neutron can be found to be in either the neutron or mirror neutron state. The probability per neutron of being found in the mirror neutron state is

$$p = \frac{2\varepsilon^2}{(\Delta E + V_F)^2 + 4\varepsilon^2 + \hbar^2\Gamma^2/4}. \tag{5.1}$$

The ε is the coupling parameter between the matter and mirror matter state, the strength of the interaction. ΔE is the energy difference between the two branes in consideration while V_F is the optical potential of the media the neutron system is passing through, specifically the optical potential that the neutron sees. The collision rate of neutrons with nuclei, Γ, is

$$\Gamma = v\Sigma_S = v\sigma_S \frac{\rho N_A}{M}$$

where v is the neutron's velocity (assuming that the nuclei can be considered as being "at rest"), Σ_S is the macroscopic cross-section of the scattering material, σ_S is the microscopic cross-section of the scatterer, ρ is the material's density, M is the material's molecular weight, and N_A is Avogadro's number. It is not stated here but σ_S is a function of temperature (and is the governing factor in why U-235 reactors are "thermal" reactors to optimize between fission and engineering constraints). To probe for the transformation from neutron to mirror neutron could require a high neutron flux and a low background in order to be able to "play the odds" for a transformation in great enough numbers that they could even be detected above the background as well as minimizing the background so that any signal would have the greatest likelihood of detection.

5.3 The ILL Reactor And Beamline H11

At the Institut Laue Langevin (ILL) in Grenoble, France, the STEREO neutrino experiment located at the High Flux Reactor (RHF) is an experiment that was designed to detect the presence of sterile neutrinos for the purpose of investigating the cause of the Reactor Antineutrino Anomaly. Much like the HFIR at ORNL, the RHF is a research reactor that generates the neutron flux through the fission of a core compoased of 95%-enriched uranium with the remaining 5% being either structural (such as aluminum) or for fission control (such as boron). The reactor is rated for 58.3 $\mathrm{MW_{th}}$, though it is instead run at 53 $\mathrm{MW_{th}}$ in order to optimize fuel cycle and reactor operations and utilizes heavy water (D_2O) in an aluminum vessel as the neutron reflector and moderator. Surrounding this vessel is a larger volume of light water (H_2O). The "heavy" concrete barrier used to contain the water and reactor is doped with boron (most likely in the form of mineral aggregate frits) as an extra layer of biological shielding. While the STEREO experiment sits along the direction of the H7 beamline, the beamline is plugged (with heavy concrete and a aluminum & B_4C composite) as the experiment does not require a beam from the reactor.

5.4 Use of Neutrino Experiments for Identifying Mirror Neutron Transitions

All details about the detector in this and the detector section §5.5 are from [2], the paper describing the detector itself and the conditions it was placed in.

As neutrino detectors needs to be heavily shielded to keep background levels tolerable, such detectors can be well-suited to being utilized for sensitive neutron regeneration experiments. Such detectors need a method to discriminate between "background" (such as normal neutrons penetrating or cosmic-muon signals) and "signal" (those neutrons that are possibly regenerated from mirror neutrons). In the case of the STEREO neutrino detector, the "signals" are the prompt positron-electron annihilation and subsequent neutron capture that come from the inverse beta decay [2]:

$$\bar{\nu}_e + p \rightarrow e^+ + n.$$

Discounting those counts that do not match the above criterion of "prompt followed by delayed" and that occur within some window of time ($\pm 400\mu$s) [3] between another event, in this way, the STEREO neutrino detector was employed to count possibly-regenerated neutrons.

5.5 The STEREO Neutrino Detector

5.5.1 The Shielding

The detector has about 65 tons of passive shielding, most of the mass being a lead outer layer for the γ-rays with a 5% borated polyethylene liner meant to capture stray external neutrons. On the top of the detector (outside the lead shielding), there is a water Cerenkov muon veto chamber with attendant photomultipliers. Underneath the lead and polyethylene there is a layer of mu-metal that surrounds the entirety of the detector "proper". All of this shielding supported within a "soft" iron frame, itself covered in B_4C. This frame is made of a low-impurity, annealed iron that does not retain magnetization well in order to help control stray magnetic fields surrounding the detector (such as from neighboring experiments). Allemandou et al. report that, despite all this shielding used on the detector, the largest contribution to the uncertainty (and thus the greatest limiting factor to their analysis) is the reactor induced background [3].

5.5.2 The Detection Vessel

The detector itself consists of six cells of Gd-doped liquid scintillator surrounded by four cells of undoped liquid scintillator (used for background discrimination and signal detection). There are 48 photomultipliers on top that are specified for the greatest sensitivity in the wavelength region of the scintillation light emission ($\sim$400 nm). All this is contained in a stainless-steel vessel.

5.5.3 The Event Signature

The delayed coincidence between a prompt positron event and a subsequent capture of thermal neutron (such as on the Gd) are the signature used to discriminate the antineutrinos from the majority of the background events. Those events that register as only a neutron capture (such as on hydrogen or gadolinium) or as a gamma ray (such as from a muon cosmic event) are rejected. Further, data was only considered when an external BF_3 counter measured < 5 neutrons per second in the detector vicinity. This corresponds to the "quietest" parts of the data measured [3].

5.5.4 General Form of Comparison Equation

To compute the estimate of transformation probability that could be expected from the experiment, the equation

$$\Gamma_i = N_1 N_2 p_1 p_2 \int_\Omega \Phi(\vec{r}) d^3 r \tag{5.2}$$

where Γ_i is the detection rate in the detector cell i (the output of the detector), N_1, N_2 are the number of scattering events in the medium the initial transformation occurs in (N_1) and the the same for the medium of final transformation (N_2), p_1 and p_2 are the probabilities of transformation in the corresponding medium, $\Phi(\vec{r})$ is the thermal neutron flux at a given position $\vec{r}$, and Ω_i is the relevant volume (i.e., detector cell i) to take the integral over. Given that the detector is ∼10 m away from the detector and the solid angle of each detector cell presented to the reactor core does not change appreciably regardless which cell is chosen for the analysis, and assuming that the thermal neutron flux is approximately constant for the entire volume of each detector cell, Eq. 5.2 can be simplified to

$$\Gamma_i = N_1 N_2 p_1 p_2 \Phi(\vec{r_i}) \Omega(\vec{r_i}) r_i \tag{5.3}$$

where $\Phi(\vec{r_i})$ is the thermal neutron flux at the face of detector cell i at distance $\vec{r_i}$, $\Omega(\vec{r_i})$ is the solid angle the detector cell face subtends, and r_i is the distance to detector cell i's face from the reactor core.

5.6 Simulation of Transition Effects via Diffusion

The STEREO collaboration had the benefit of much simulation: MCNPX simulations with models provided by the ILL, FIFRELIN and GEANT4 simulations of the detector and expected fluxes, as well as four years of data collection from 2016 to 2020 to evaluate [3]. This work did not have this benefit. However, not all of the previous is necessary in order to determine whether or not the STEREO collaboration has overlooked an important detail. While accurate simulations require accurate models underpinning them, a sufficient "sketch" can be obtained by even a simple neutron transport simulation.

The important detail that would be gained from even a simple simulation would be the number of collisions that the neutron undergoes. As each scattering event is a measurement on the neutron-mirror neutron system, the average number of measurements provides insight into how likely the neutron is to oscillate at each given collision. Materials with a large number of scatterings could possibly contribute appreciably more to the transformation while those with fewer might be less useful.

5.6.1 Neutron Diffusion

The transport of neutrons from the core of a nuclear reactor to some external region is described by Boltzmann's transport equation which has the form

[?]

$$\left[\frac{\partial}{\partial t} - \frac{\partial U}{\partial \vec{q}_1} \cdot \frac{\partial}{\partial \vec{p}_1} + \frac{\vec{p}_1}{m} \cdot \frac{\partial}{\partial \vec{q}_1}\right] f_1 = \left(\frac{\partial f_1}{\partial t}\right)_{coll} \tag{5.4}$$

where f_1 is a single-particle density function of momentum $\vec{p}_1$ and position $\vec{q}_1$, $\partial f_1/\partial t$ is the change in the density function as a function of time, and $\partial U/\partial \vec{q}_1 \cdot \partial/\partial \vec{p}_1$ & $\frac{\vec{p}_1}{m} \cdot \frac{\partial}{\partial \vec{q}_1}$ are streaming terms relating to the motion of the neutrons. These streaming terms would contains such as any sources and sinks (in the gradient term) as well as changes due to the motion (the momentum gradient term).

However, beyond the generation of the free neutron from the initial fission process, there are no significant sources in the reactor, meaning the gradient term can be neglected. Further, as neutrons are electrically neutral, there are no sufficiently-strong magnetic fields to influence the trajectory of the neutron, meaning the neutrons have no influence on each other as they diffuse throughout the reactor.

and because the density of neutrons is so low as to not require interparticle interactions, there is no need to account for electromagnetic effects nor neutron-neutron interactions. With these points in mind, a simple diffusion simulation that propagated the neutrons through the materials of the reactor to the distance of the detector was written in Fortran, taking into account the real and imaginary parts of the nuclear potentials of the materials encountered.

5.6.2 Random Walk Simulation Results

The simulation predicts that a neutron will scatter off an atom or molecule approximately 25 times in D_2O which is similar to values found in references and thermalize in the D_2O in approximately 112 collisions. In H_2O, the simulation predicts approximately 36 collisions. Shown in **Figure 5.1** is the path one of the simulated neutrons took.

Contributions of other materials can be computed but were considered as unnecessary: the majority had either scattering potentials too low to be meaningful in comparison such as in iron-based components, aluminum, lead, or were doped with a powerful neutron absorber as a part of biological shielding (boral, heavy concrete, borated PE and rubber). In these materials, low scattering potentials and possibly large absorption potentials render any significance of the transformation probability negligible at best. These values for the number of scattering events determine the value of N_1 in Eq. 5.3. Natural mirror matter abundances are so low as to be negligible (refer back to Eq. 1.3 where the mirror matter contribution is assumed 0). Transformation back into regular matter is assumed to be from the neutron state interacting with regular matter, resulting in a measurement of the system as a neutron. Thus, $N_2 = 1$ is assumed.

5.6.3 Reactor Flux Calculations

The Argonne National Lab (ANL) released a report in 2014 on the feasibility of converting the RHF from highly-enriched uranium to low-enriched uranium in a bid to minimize possibilities of nuclear proliferation [7]. However, more relevant to this work is the inclusion of multiple plots (**Figs. 5.2**, **5.3**, and **5.4**) depicting the measurements of the flux and the national lab's calculations thereof.

Starting with the plot presented in **Fig. 5.2**, the thermal neutron flux was approximated using a digitizer (Ref. [28]) to record the data points of the green dots (corresponding to the thermal neutrons). For the axial flux, the data points of the plots of **Figures 5.3** and **5.4** were recorded by eye. From this the data points were interpolated using the Fortran PCHIP [12] library in order to make them more convenient for sampling. **Figures 5.5** and **5.6** show the simulated flux from the reactor core and the interpolated flux away from the reactor core.

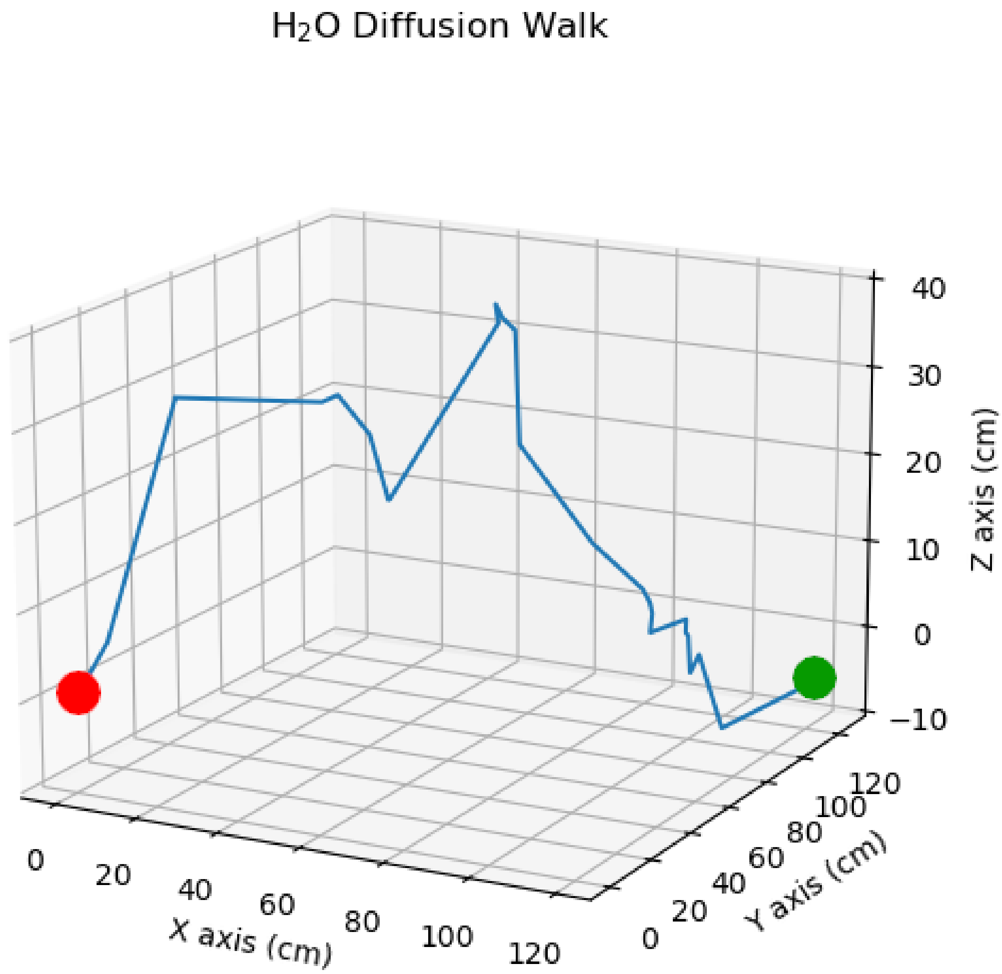

Figure 5.1: An example of the path a neutron takes as it diffuses through H_2O. The red circle on the left is the start of the walk while the green circle on the right is the end after having traveled through the light water layer in the reactor.

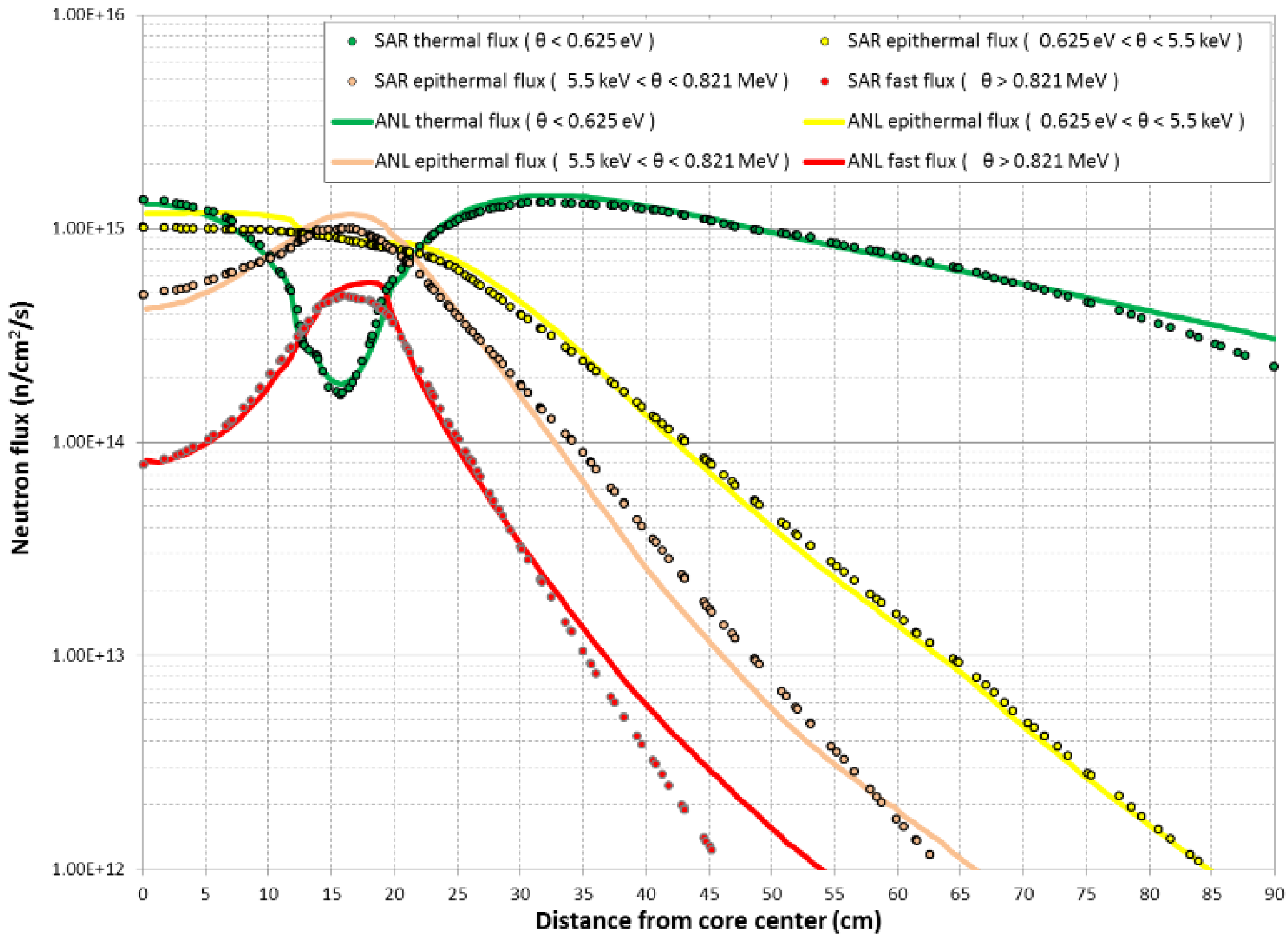

Figure 5.2: Figure 4.2-3 of [7].

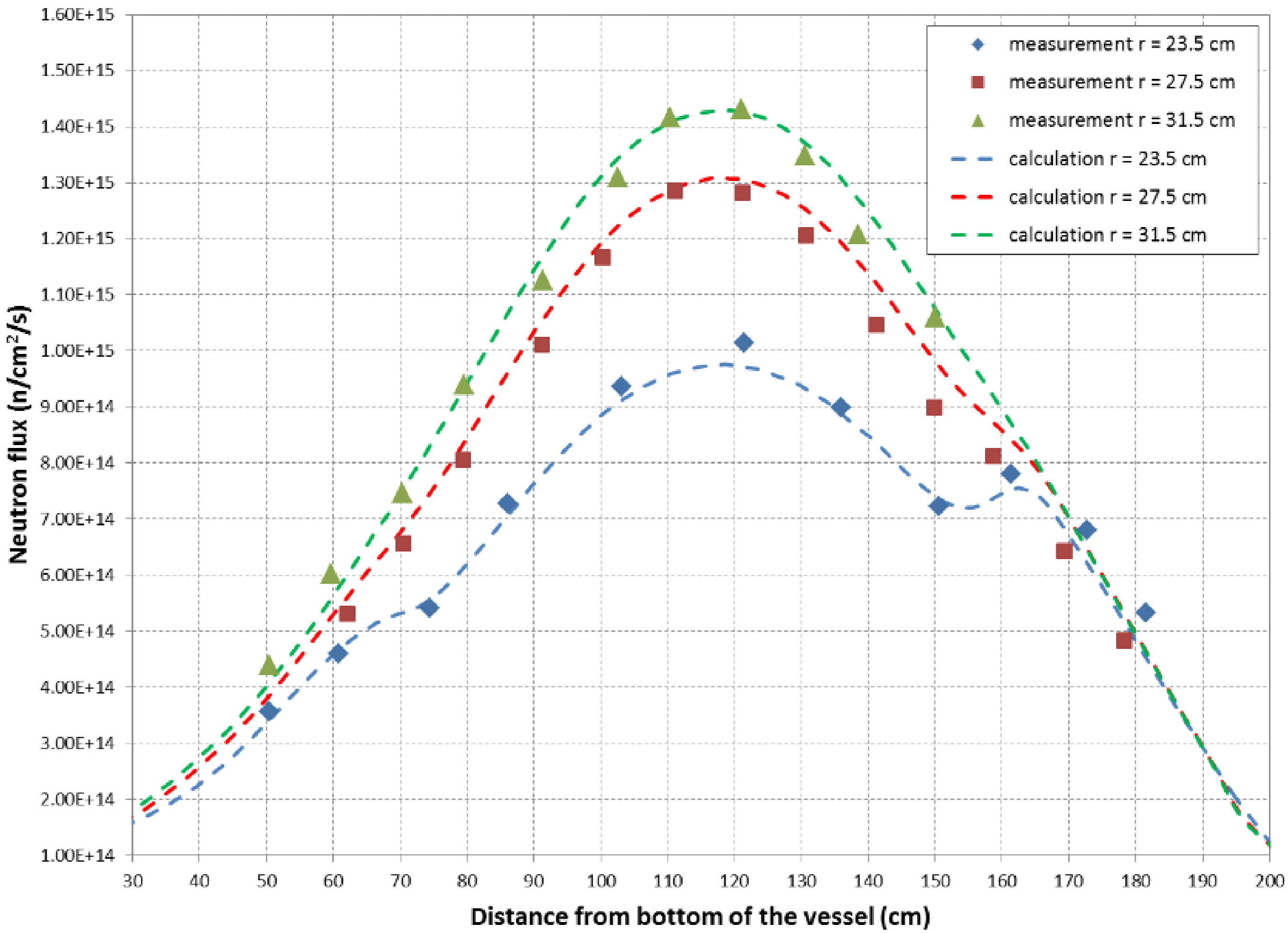

Figure 5.3: Figure 4.2-1 of [7].

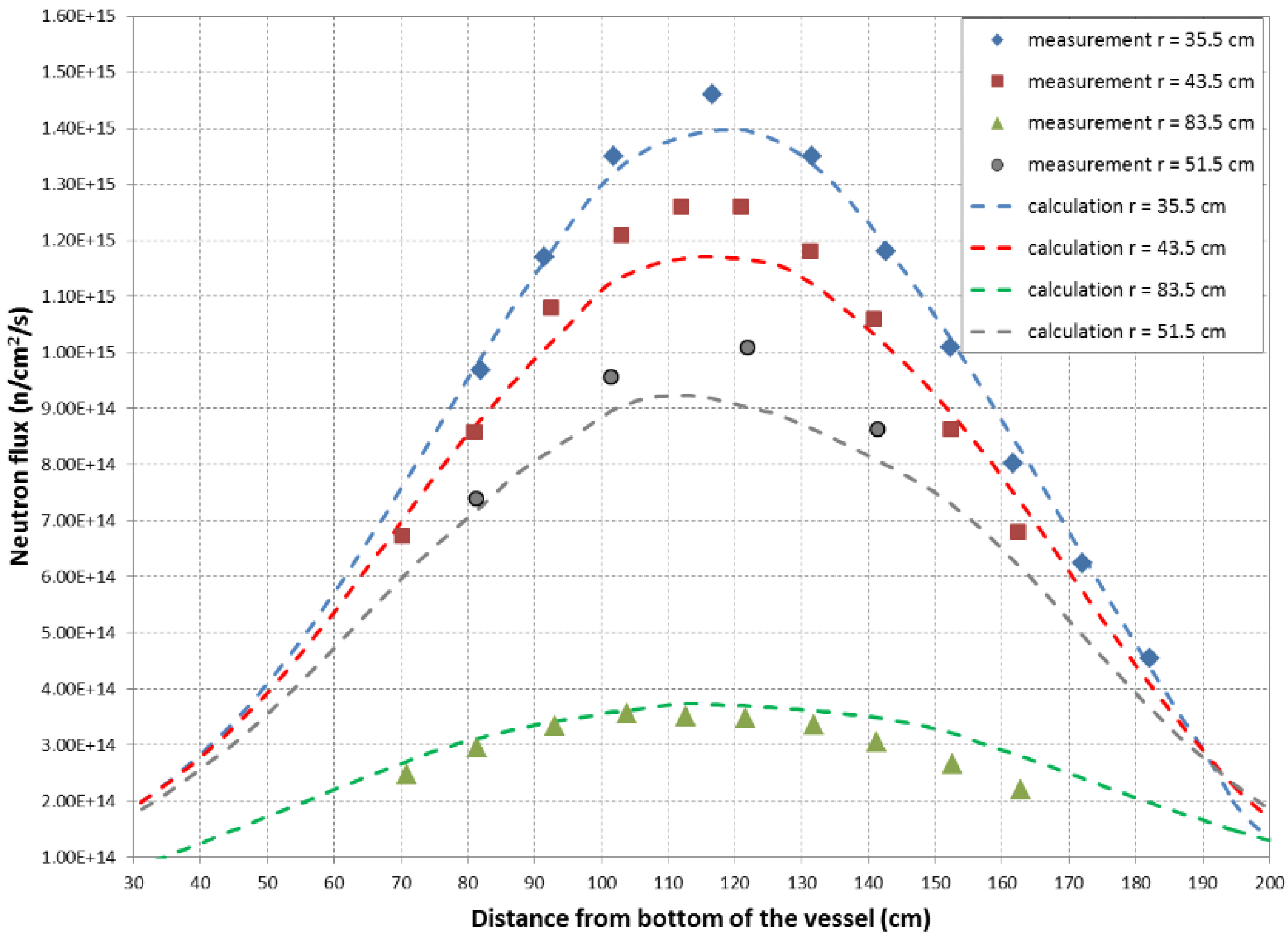

Figure 5.4: Figure 4.2-2 of [7].

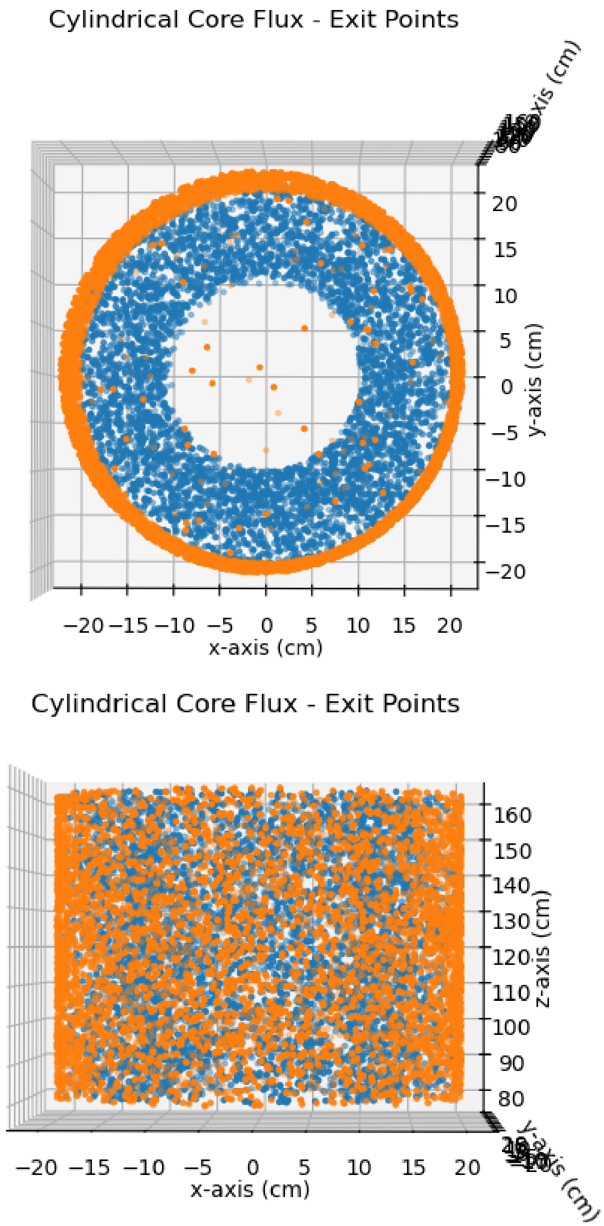

Figure 5.5: Plots showing the first 5000 neutrons exiting the core region. 10^6 neutrons were generated to verify that the majority of the simulated neutron flux from the reactor was indeed coming from the sides of the fuel and not escaping from the top of the top. Blue dots correspond to where the neutrons are emitted during a fission event within the volume of the annulus of the fuel while the orange are where the neutrons exited the region of the volume of the cylinder.

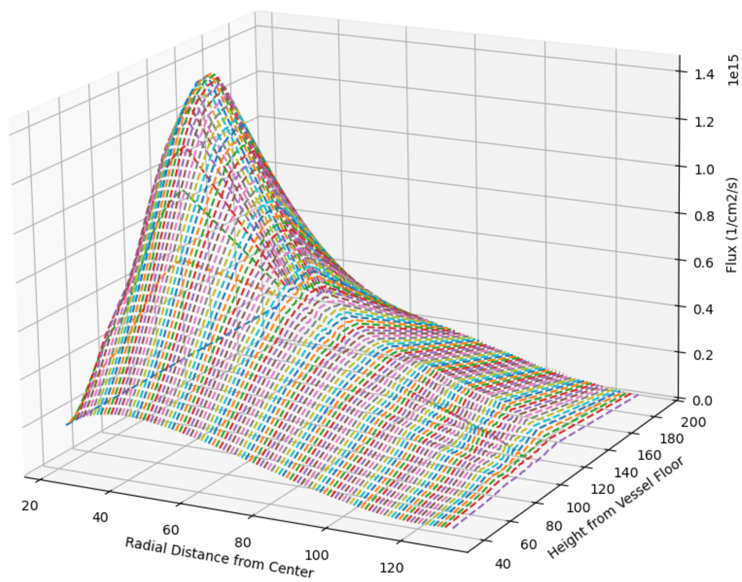

Figure 5.6: Flux from the data interpolated from Figs. 5.2, 5.3, and 5.4.

5.7 Final Results

Calculations of the limit STEREO presents are on the order of within 10× what is plotted in Figure 3 of [3], often only a multiplicative factor of 3 different. While the contribution from the light water of the reactor would have made a contribution that would have appeared in **Figures 3.9** and **4.4** on the $\Delta m < 0$ plots, the contribution it would have had to the claimed limit is not appreciable as the optical potential of water is ~$1/10^{\text{th}}$ that of D_2O. The fact that the optical potential of light water is an order of magnitude weaker in strength means that it falls in a region of less sensitivity negating any advantage that the additional scattering events would have produced. While the "accuracy" of these results leaves something to be desired, it is not unreasonable to consider that the original paper had the support of the RHF staff as well as the computational time and expertise in specific modeling software that was not available to this analysis that would aid in the accuracy of the simulations described here.

Chapter 6

Conclusion

The hunt for the explanation for dark matter has taken a prominent seat in the minds of many physicists. At the moment, the only results that have come from a multitude of experiments are limits on the permitted parameter space of the various theories though not for a lack of experiment time dedicated. For my part, I have analyzed results from the data taken in 2020 at the SNS for background subtraction, intensity determination and characterization, and numerical simulations of expected results. As well, as a part of the collaboration that took the 2024 data set at the HFIR, I have likewise contributed to background determination and numerical simulations of expected results. Finally, as a third-party, I have reviewed the claims of the STEREO collaboration regarding their probability limits and have found my work to be in-line with their stated claims.

Bibliography

[1] Abe, T., Kakizaki, M., Matsumoto, S., and Seto, O. (2012). Vector wimp miracle. *Physics Letters B*, 713:211 – 215. vi

[2] Allemandou, N., Almazán, H., Sanchez, P. d. A., Bernard, L., Bernard, C., Blanchet, A., Bonhomme, A., Bosson, G., Bourrion, O., Bouvier, J., Buck, C., Caillot, V., Chala, M., Champion, P., Charon, P., Collin, A., Contrepois, P., Coulloux, G., Desbrières, B., Deleglise, G., Kanawati, W. E., Favier, J., Fuard, S., Monteiro, I. G., Gramlich, B., Haser, J., Helaine, V., Heusch, M., Jentschel, M., Kandzia, F., Konrad, G., Köster, U., Kox, S., Lahonde-Hamdoun, C., Lamblin, J., Letourneau, A., Lhuillier, D., Li, C., Lindner, M., Manzanillas, L., Materna, T., Méplan, O., Minotti, A., Monon, C., Montanet, F., Nunio, F., Peltier, F., Penichot, Y., Pequignot, M., Pessard, H., Piret, Y., Prono, G., Quéméner, G., Real, J.-S., Roca, C., Salagnac, T., Sergeyeva, V., Schoppmann, S., Scola, L., Scordilis, J.-P., Soldner, T., Stutz, A., Tourres, D., Vescovi, C., and Zsoldos, S. (2018). The

STEREO experiment. *Journal of Instrumentation*, 13(07):P07009–P07009. Publisher: IOP Publishing. 23, 63, 64

[3] Almazán, H., Bernard, L., Blanchet, A., Bonhomme, A., Buck, C., del Amo Sanchez, P., El Atmani, I., Labit, L., Lamblin, J., Letourneau, A., Lhuillier, D., Licciardi, M., Lindner, M., Materna, T., Méplan, O., Pessard, H., Pignol, G., Réal, J.-S., Ricol, J.-S., Roca, C., Rogly, R., Salagnac, T., Sarrazin, M., Savu, V., Schoppmann, S., Soldner, T., Stutz, A., and Vialat, M. (2022). Searching for Hidden Neutrons with a Reactor Neutrino Experiment: Constraints from the STEREO Experiment. *Physical Review Letters*, 128(6):061801. Publisher: American Physical Society. 43, 60, 64, 65, 67, 77

[4] Ban, G. and et al. (2023). Search for neutron-to-hidden-neutron oscillations in ultracold neutron beam. *Physical Review Letters*. 43

[5] Berehiani, Z. (2019). Neutron lifetime puzzle and neutron – mirror neutron oscillation. *Eur. Phys.J. C*, 79. 10, 11

[6] Berezhiani, Z. and Bento, L. (2006). Neutron–mirror-neutron oscillations: How fast might they be? *Phys. Rev. Lett.*, 96:081801. 4, 7

[7] Bergeron, A., Dionne, B., and Calzavara, Y. (2014). Neutronics conversion analysis of the laue-langevin institute (ill) high flux reactor (rhf). 70, 72, 73, 74

[8] Broussard, L., Barrow, J., DeBeer-Schmitt, L., Dennis, T., Fitzsimmons, M., Frost, M., Gilbert, C., Gonzalez, F., Heilbronn, L., Iverson, E., Johnston, A., Kamyshkov, Y., Kline, M., Lewiz, P., Matteson, C., Ternullo, J., Varriano, L., and Vavra, S. (2022). Experimental search for neutron to mirror neutron oscillations as an explanation of the neutron lifetime anomaly. *Physical Review Letters.* 22, 41, 55

[9] Chowdhury, T. and Ipek, S. (2023). Neutron lifetime anomaly and big bang nucleosynthesis. *Canadian Journal of Physics*, pages 96–99. 22

[10] Cottingham, W. D. and Greenwood, D. A. (1998). *An Introduciton to the Standard Model of Particle Physics.* Cambridge University Press. 1

[11] Foot, R. (2002). Does mirror matter exist? 4

[12] Fritsch, F. N. (1985). Pchip, piecewise cubic hermite data interpolation. 70

[13] Gninenko, S. and Krasnikov, N. (2025). Search for mirror hidden sector with neutral kaons at na64. *Phys.Rev.D.* 20

[14] Gonzalez, F., Fries, E., Cude-Woods, C., Bailey, T., Blatnik, T., Broussard, L., Callahan, N., Choi, J., Clayton, S., and UCN τ Collaboration (2021). Improved neutron lifetime measurement with ucnτ. *Physical Review Letters.* 22, 43

[15] Gonzalez, F. M., Rock, C., Broussard, L. J., DeBeer-Schmitt, L., Frost, M. J., Heilbronn, L., Iverson, E. B., Kamyshkov, Y., Kline, M., Milstead,

D., Powers, D., Rogers, J., Santoro, V., and Vavra, S. (2024). Improved limits on $n \rightarrow n'$ transformation from the spallation neutron source. 27, 28, 38, 39

[16] Good, R., Matsen, R., Muller, F., Piccioni, O., Powell, W., White, H., Fowler, W., and Birge, R. (1961). Regeneration of neutral k mesons and their mass difference. *Phys.Rev.* 8, 20, 21

[17] Hui, L. (2021). Wave dark matter. *Annual Review of Astronomy and Astrophysics*, 59(Volume 59, 2021):247–289. vi

[18] Inoue, K. T., Minezaki, T., Matsushita, S., and Nakanishi, K. (2023). Alma measurement of 10 kpc scale lensing-power spectra toward the lensed quasar mg j0414+0534. *The Astrophysical Journal*, 954(2):197. 2, 3

[19] Iwamoto, O., Iwamoto, N., Kunieda, S., Minato, F., Nakayama, S., Abe, Y., and et al. (2023). Japanese evaluated nuclear data library version 5: Jendl-5. *J. Nucl. Sci. Technol.*, 60:1–60. 29

[20] Kamyshkov, Y., Ternullo, J., Varriano, L., and Berezhiani, Z. (2022a). Neutron-mirror neutron oscillations in absorbing matter. *Symmetry*, 14(2). 11

[21] Kamyshkov, Y., Ternullo, J., Varriano, L., and Berezhiani, Z. (2022b). Neutron-Mirror Neutron Oscillations in Absorbing Matter. *Symmetry*,

14(2):230. Number: 2 Publisher: Multidisciplinary Digital Publishing Institute. 33

[22] Myers, S. and Schopper, H. (2020). *Particle Physics Reference Library, Volume 3: Accelerators and Colliders*. Springer Cham. 24

[23] nEDM Collaboration at PSI (2021). A search for neutron to mirror-neutron oscillations using the nedm apparatus at psi. *Journal of Physics Letters B*. 22, 43

[24] Oak Ridge National Laboratory (2025). Magnetism reflectometer. 25

[25] Peskin, M. E. and Schroeder, D. V. (2019). *An Introduction to Quantum Field Theory*. CRC Press. 1

[26] Petit, F. and Sarrazin, M. (2005). Quantum dynamics of massive particles in a non-commutative two-sheeted space–time. *Physics Letters B*, 612. 16

[27] Pugnat, P., Ballou, R., Deferne, G., Duvillaret, L., Finger Jr., M., Finger, M., Flekova, L., Hosek, J., Husek, T., Jary, V., Jost, R., Kunc, S., Macuchova, K., Meissner, K., Morville, J., Romanini, D., Seimko, A., Slunecka, M., Sulc, M., Vitrant, G., and Zicha, J. (2015). Osqar chase proposal. 8, 21

[28] Rohagi, A. (2025). Web plot digitizer. 70

[29] Romanino, A. (2009). The Standard Model of Physics. In *Proceedings of the Baikal summer JINR-ISU school on physics of elementary particles and astrophysics 2009*. 1

[30] Rubin, V. C. and Ford, W. Kent, J. (1970). Rotation of the Andromeda Nebula from a Spectroscopic Survey of Emission Regions. , 159:379. 2, 3

[31] Sarrazin, M. and Petit, F. (2012). Brane matter, hidden or mirror matter, their various avatars and mixings: many faces of the same physics. *Eur. Phys. J. C*. 60

[32] Sarrazin, M., Pignol, G., Lamblin, J., Petit, F., Terwagne, G., and Nesvizhevsky, V. V. (2015). Probing the braneworld hypothesis with a neutron-shining-through-a-wall experiment. *Phys. Rev. D*, 91:075013. 16, 18

[33] Sato, T., Iwamoto, Y., Hashimoto, S., Ogawa, T., Furuta, T., Abe, S., Kai, T., Matsuya, T., Matsuda, N., Hirata, Y., Sekikawa, T., Yao, L., Tsai, P., Ratliff, H., Iwase, H., Sakaki, Y., Sugihara, K., Shigyo, N., Sihver, L., and Niita, K. (2024). Recent improvements of the particle and heavy ion transport code system - phits version 3.33. *J. Nucl. Sci. Technol.*, 61:127–135. 26

[34] Schwartz, M. D. (2014). *Quantum Field Theory and the Standard Model*. Cambridge University Press. 1

[35] Stasser, C., Terwagne, G., Lamblin, J., Méplan, O., Pignol, G., Coupé, B., Kalcheva, S., Van Dyck, S., and Sarrazin, M. (2021). Probing neutron-hidden neutron transitions with the MURMUR experiment. *The European Physical Journal C*, 81(1):17. arXiv:2007.11335 [hep-ex, physics:hep-ph, physics:nucl-ex, physics:physics]. 23, 43, 60

[36] Zwicky, F. (1937). On the Masses of Nebulae and of Clusters of Nebulae. , 86:217. 2, 3

Vita

Cary Rock was born in Orange, California in September of 1992 to Alan and Suzanne Rock. He attended Santiago Canyon College, the local community college from 2010 to 2016 for engineering and then later physics. He then attended the California State Polytechnic University, Pomona, from 2016 to 2018 earning a B.Sci. in physics. In 2018 he was accepted to the University of Tennessee, Knoxville's graduate program for physics. After being a graduate teaching assistant for three years, he joined Adrian Del Maestro's group for theoretical condensed matter physics for a year and received his Master's degree. After this year, in 2022, he joined Yuri Kamyshkov's experimental particle physics group to analyze mirror neutron experiment data. Upon graduation, Cary took a short vacation.